Karlsruhe Institute of Technology

INSTITUTO TECNOLOGICO DE BUENOS AIRES
UNIVERSIDAD PRIVADA

CFD Simulation of a Hydrogen Explosion Experiment in an ISO Container

An der Fakultät für Maschinenbau des Karlsruher Instituts für Technologie eingereichte

Masterarbeit

zur Erlangung des akademischen Grades

Master of Science Maschinenbau

(M.Sc. Maschinenbau)

Vorgelegt von

Philipp Weber

Betreut von:

Prof. Dr. Thomas Schulenberg
Dr. Thomas Jordan
Dr. Alexei Kotchourko

Eidesstattliche Versicherung

Ich versichere, dass ich die vorliegende Arbeit selbständig und ohne Benutzung anderer als der angegebenen Hilfsmittel angefertigt habe. Alle Stellen, die wörtlich oder sinngemäß aus Veröffentlichungen oder anderen Quellen entnommen sind, sind als solche eindeutig kenntlich gemacht. Die Arbeit ist in gleicher oder ähnlicher Form noch nicht veröffentlicht und noch keiner Prüfungsbehörde vorgelegt worden.

Karlsruhe, den 15. Dezember 2017

Zusammenfassung

Das EU-Projekt HySEA widmet sich der Verminderung von Explosionsrisiken durch Deflagrationsentlüftung industrieller Wasserstoff-Anlagen. Zur Weiterentwicklung und Validierung von Verbrennungsmodellen wurden verschiedene Experimente in 20-Fuß ISO Containern durchgeführt. Die erste Testkampagne beinhaltete die Blindvorhersage von zwei mageren vorgemischten Versuchsanordnungen. Die Wasserstoff-Gruppe des IKET reichte auf der Basis des institutseigenen COM3D Codes eine Modellvorhersage ein, welche keine zufriedenstellende Übereinstimmung mit den Experimenten zeigte. Das Ziel dieser Arbeit war daher, die Vorhersagbarkeit des CFD Codes anhand nachgelagerter Berechnungen zu verbessern. Im Hinblick auf den Prozess der Flammenbeschleunigung wurden insbesondere die Rolle thermodiffusiver Instabilität und das Modell turbulenter Flammengeschwindigkeit analysiert und geklärt. Daraus folgte die Weiterentwicklung des numerischen Modells des Übergangs von laminarer zu turbulenter Flammengeschwindigkeit sowie dessen Implementierung in den COM3D Code. Validierungsrechnungen zeigten erfolgreiche Übereinstimmung mit den experimentellen Ergebnissen. Dies stellt einen ersten Schritt zur Erweiterung des Anwendungsspektrums des Codes für weitere Verbrennungsszenarien dar.

Abstract

The EU project HySEA is dedicated to explosion risk reduction by deflagration venting of industrial hydrogen installations. In 20-foot ISO containers, several experiments have been conducted to provide data for combustion model improvement and validation. The first experimental campaign included a blind-prediction study concerning two lean premixed configurations. The hydrogen research group of IKET submitted a model prediction based on the in-house code COM3D. The experimental results were not matched. Therefore, the objective of this thesis was to improve the predictability of the CFD code by carrying out post-blind simulations. Over the course of this work, the roles of thermodiffusive instability and the turbulent flame speed model in the process of flame acceleration were analyzed and clarified. As a consequence, the numerical model for the transition from laminar to turbulent flame speed was developed and implemented in the COM3D code. Validating simulations demonstrated satisfactory agreement compared to the experimental results. This represents a first step toward extending the applicability of the code to a wider range of combustion scenarios.

Contents

Nomenclature

Abbreviations

BC	Boundary condition
CAD	Computer Aided Design
CFD	Computational Fluid Dynamics
DDT	Deflagration to Detonation Transition
DNS	Direct Numerical Simulation
FA	Flame acceleration
GUI	Graphical user interface
HySEA	Improving Hydrogen Safety for Energy Applications through pre-normative research on vented deflagrations
IKET	Institute for Nuclear and Energy Technology
LES	Large Eddy Simulation
RANS	Reynolds Averaged Navier-Stokes
TDI	Thermodiffusive Instability

Dimensionless numbers

Da	Damköhler number
Ka	Karlovitz number
Le	Lewis number
Re_t	Turbulent Reynolds number

Greek symbols

α	Species
α	Thermal diffusivity
β	Instability model exponent
δ	Flame thickness
δ_{ij}	Kronecker delta
λ	Thermal conductivity
μ	Dynamic viscosity
ν	Kolmogorov length scale
ω	Reaction rate
ϕ	Fuel-to-air equivalence ratio
ρ	Density
σ_{ij}	Viscous stress tensor
τ_ν	Kolmogorov time scale
τ_L	Laminar reaction time scale
τ_t	Turbulent transport time scale
ε	Viscous dissipation
Ξ	Surface wrinkling factor

Latin symbols

$\overline{k}$	Wavenumber
A	Turbulence enhancing factor
D	Molecular diffusivity
e	Total specific energy
E_a	Activation energy

f	Progress variable
g	Gravitational acceleration
H_K	Forced combustion rate
j	Diffusion flux
k	Turbulent kinetic energy
k_r	Rate constant
L	Integral length scale
l_n	Turbulent eddy size
n	Reaction order
p	Pressure
q	Heat flux
R	Flame radius
R	Universal gas constant
R_0	Critical radius of instability onset
S_L	Laminar flame speed
S_t	Turbulent flame speed
S_{ij}	Rate of strain tensor
S_{ql}	Quasi-laminar flame speed
T	Temperature
t	Time
u	Velocity
u'	RMS turbulent velocity
Y	Mass fraction

List of Figures

1 Introduction

1.1 Motivation

In order to reduce greenhouse gas emissions, fossil energy sources need to be replaced by more sustainable alternatives. This results in the implementation of renewable energies and also affects transportation. Hydrogen represents one promising way to connect the energy and mobility sector. Concretely, excess wind and solar energy is stored chemically and can be used in fuel cells or internal combustion engines.
However, hydrogen technology still has to overcome several challenges to prove its suitability for widespread use and acceptance in society. In this context, hydrogen safety is a crucial factor. Owing to its characteristic properties, such as the broad flammability range and very low ignition energy, explosions pose a considerable danger for hydrogen installations.
Equipment for hydrogen energy applications is frequently placed in containers or smaller enclosures. The consequences of explosions are usually mitigated by deflagration venting. In order to further investigate the explosion pressures of large-scale containers and the appropriate design of corresponding mitigation concepts, the HySEA (*Improving Hydrogen Safety for Energy Applications through pre-normative research on vented deflagrations*) project was originated. One of the main objectives was to provide experimental data for CFD code development and validation.
The experimental campaign of HySEA also includes a blind-prediction study, where several institutes submitted model predictions before the completion of the actual experiments. The hydrogen research group of the Institute of Nuclear and Energy Technologies (IKET) participated with their in-house CFD code COM3D. The simulation results did not match the experimental data, which gave rise to the idea of performing post-blind calculations.

1.2 Aim and description of the work

The main objective of this thesis is to reproduce the experiments of the first HySEA blind-prediction study with the reactive CFD code COM3D and to understand why the submitted model prediction did not yield satisfying results. Another issue to be investigated is the applicability of the code to further cases concerning slow deflagrations, possibly allowing blind-predictions in the future. It has to be kept in mind that COM3D is primarily developed and used for the calculation of fast deflagrations and deflagration to detonation transition phenomena.
In this work, the first two experiments of the HySEA project are considered: two different deflagration venting scenarios in an ISO container with the same lean (15% hydrogen) premixed hydrogen-air mixture. In the first configuration, the container is left empty, while the second set-up includes a bundle of gas bottles as an obstacle. The computed overpressure generated by the explosion is compared with the experimental values.
In this work, the experimental set-ups and respective results are presented. Then, several simulation approaches with the existing COM3D code are displayed. The successful calculation is achieved by varying different combustion and flame speed model parameters. This procedure leads to a hypothesis about the possible source of the discrepancy between the experiment and the model prediction. Consequently, code development is proposed.
At first, the principles of turbulent combustion, including a short introduction to instabilities and vented deflagrations, are presented. Chapter 3 deals with the HySEA project and the results of the blind-prediction study. Chapter 4 gives information on the current structure of the COM3D code, its most important combustion model and the code modifications suggested in this work. In chapter 5, the simulation procedure in COM3D is shown, implying the geometric model and an overview of the most important calculation approaches. In chapter 6, the results of this work are discussed. In the last chapter (7), conclusions are drawn and proposals for possible subsequent research are made.

2 Basics of turbulent combustion

Combustion is a multi-physical phenomenon, which comprises chemical reactions as well as complex interactions between flame front and flow field.

2.1 Governing equations

Meaningful simulation of combustion phenomena requires the numerical solution of the reactive Navier-Stokes equations. The motion of a reactive flow is described by the conservation of mass (Eqn. 2.1), momentum (Eqn. 2.2), energy (Eqn. 2.3) and species (Eqn. 2.4). In tensor notation, these equation are formulated as:

$$\frac{\partial \rho}{\partial t} + \frac{\partial \rho u_j}{\partial x_j} = 0, \tag{2.1}$$

$$\frac{\partial \rho u_i}{\partial t} + \frac{\partial}{\partial x_j}(\rho u_i u_j + p\delta_{ij}) = \frac{\partial \sigma_{ij}}{\partial x_j} + \rho g_i, \tag{2.2}$$

$$\frac{\partial \rho e}{\partial t} + \frac{\partial}{\partial x_j}((\rho e + p)u_i) = \frac{\partial}{\partial x_i}(u_j \sigma_{ij} - q_i) + \rho g_i u_i, \tag{2.3}$$

$$\frac{\partial \rho Y_\alpha}{\partial t} + \frac{\partial \rho Y_\alpha u_i}{\partial x_i} = \frac{\partial j_i}{\partial x_i} + \rho \omega_\alpha. \tag{2.4}$$

ρ denotes the density, u the velocity, p the pressure, σ_{ij} the viscous stress tensor, g the gravitational acceleration, e the total specific energy, Y_α the mass fraction of the species α, j the diffusion flux and ω_α with $\alpha = 1...N_{species}$.
For Newtonian fluids and negligible bulk viscosity, the shear stress tensor is defined as

$$\sigma_{ij} = 2\mu S_{ij} - \frac{2}{3}\mu \delta_{ij} S_{kk}, \tag{2.5}$$

where the rate of strain tensor S reads

$$S_{ij} = \frac{1}{2}(\frac{\partial u_i}{\partial x_j} + \frac{\partial u_j}{\partial x_i}). \tag{2.6}$$

The heat flux follows Fourier's law

$$q_j \approx -\lambda \frac{\partial T}{\partial x_j}, \tag{2.7}$$

with the thermal conductivity λ and the dynamic viscosity μ. Diffusion behaves according to Fick's law

$$j_i \approx -\rho D_\alpha \frac{\partial Y_\alpha}{\partial x_i}, \tag{2.8}$$

with D_α being the diffusivity of the species α.
If no turbulence or combustion models are applied, the Navier-Stokes equations need to be resolved over the entire range of time and length scales. This approach is called Direct Numerical Simulation (DNS), a computation-intensive method, which currently only allows the simulation of low Reynolds number flows and simple geometries.
Alternatively, the equations can be averaged or filtered. Typical averaging approaches result in the separation of a certain quantity ϕ into a mean and fluctuating part $\phi = \overline{\phi} + \phi'$. In COM3D, the Favre averaged Navier-Stokes equations are utilized ($\phi = \tilde{\phi} + \phi''$), which are obtained by averaging over density as $\tilde{\phi} = \frac{\int \rho(t)\phi(t)dt}{\int \rho(t)dt}$.

2.2 Chemical kinetics

Chemical reactions usually take place at speeds comparable to flow velocities. Therefore, chemical reaction kinetics are required. In reality, combustion involves a multitude of elementary reactions and intermediate products. In simulations focusing on the hydrodynamic effects of combustion, these mechanisms are frequently simplified to a one-step global reaction, containing fuel (F), oxidizer (O) and products (P). [23]

$$F + O \rightarrow P. \tag{2.9}$$

The reaction rate describes, how fast the substances involved in the combustion process are consumed or formed. For fuel and oxidizer, this yields the reaction rates:

$$\omega_F = \frac{d[F]}{dt} = \omega_O = \frac{d[O]}{dt} = -k_r [F]^{n_F} [O]^{n_O}, \tag{2.10}$$

with n_F and n_O denoting the reaction orders of fuel and oxidizer and k_r as rate constant. This rate constant is defined by an Arrhenius equation as:

$$k_r = A \cdot exp(-\frac{E_a}{RT}). \tag{2.11}$$

Equation 2.11 contains the preexponential factor A, the activation energy E_a and the universal gas constant R. Most importantly, it shows a characteristic of chemical reactions: highly non-lineal dependence on temperature. [30]

2.3 Premixed turbulent combustion

In combustion, different flame types can be distinguished. If fuel and oxidizer are mixed at the same time as they are burned, a *diffusion (or nonpremixed) flame* is formed. In the experiments considered in this work, mixing occurs prior to combustion, which leads to a *premixed flame*. Depending on the flow type, the mentioned flame types can assume either a *laminar* or a *turbulent* shape. [30] Those two regimes are further elaborated in the following subsections.

2.3.1 Laminar flames

In most practical combustion applications, the flow field turns rather quickly from laminar to turbulent. Still, the understanding of laminar flames is important, because it is fundamental for the description of turbulent flames.
Laminar flames emerge due to sufficiently weak ignition, for instance by a spark or thermal conduction by hot surfaces. They move as a combustion wave through thermal and molecular diffusion. In the case of premixed combustion, the flame propagates normal to its surface. In unconfined environments, flames expand spherically. For large radii compared to flame thickness, the flame surface can be assumed planar.
Figure 2.1 illustrates the behavior of temperature and the concentration of reactants of such a profile between unburned (u) and burned (b) state. It can be seen that heat and mass flow in opposite directions. The flame front consists of two parts: the pre-heat zone, whose width represents the majority of the flame thickness, and the reaction zone. Within the chemically inert pre-heat zone, the temperature increases downstream from its initial value T_u to T_1 due to heat conduction. Starting from T_1, heat release caused by the chemical reaction further raises the temperature up to T_b, where the reactants are completely consumed. [18]

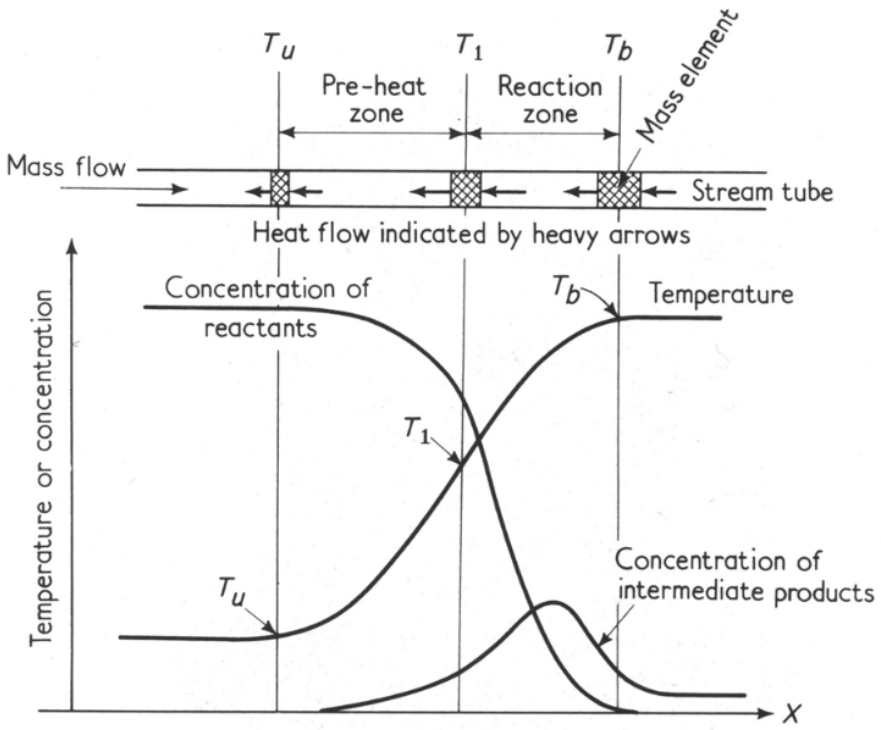

Figure 2.1: Scheme of a plane combustion wave [18]

The main characteristic of a laminar flame is its burning velocity S_L, which describes the propagation speed of the flame front in normal direction relative to the flow. It is a thermo-chemical property, that depends on the temperature in the unburned mixture T_u, the pressure p and the fuel-to-air equivalence ratio $\phi = \frac{m_{fuel}/m_{ox}}{(m_{fuel}/m_{ox})_{st}}$. The value of ϕ indicates, if the combustion is carried out at stoichiometric conditions ($\phi = 1$), with excess fuel ($\phi > 1$) or surplus oxidizer ($\phi < 1$).
Between the mentioned boundaries u and b in Fig. 2.1, the flow is accelerated due to thermal expansion. That is why the laminar burning velocity S_L is not to be confused with the flame front speed determined in the burned mixture $v_{n,b}$. Assuming constant mass flux ($\rho v_n = const.$) in normal direction leads to the expression

$$(\rho v_n)_u = (\rho v_n)_b, \tag{2.12}$$

which can be transformed into

$$v_{n,b} = v_{n,u}\,\frac{\rho_u}{\rho_b} = v_{n,u}\sigma = S_L\sigma. \tag{2.13}$$

Multiplying $v_{n,u} = S_L$ by the expansion factor σ yields the velocity $v_{n,b}$, which includes the effect of convection for flame propagation. [23]

The laminar burning velocity has been extensively determined in experiments, while numerical approaches also exist. For certain assumptions, [30] derived the analytical expression

$$S_L = \sqrt{\frac{\alpha}{\tau}}, \tag{2.14}$$

with the thermal diffusivity $\alpha = \frac{k}{\rho c_p}$ and $\tau \propto exp(-\frac{E_a}{RT})^{-1}$, which is a characteristic time of reaction proportional to Arrhenius.

2.3.2 Turbulent flames

In contrast to the laminar case, turbulent flame velocities cannot be determined as easily. There is a variety of approaches to calculate turbulent flame speed, which will be described more thoroughly in section 2.5 and chapter 4. As an introduction, this subsection deals with the basic phenomenology of turbulent flows and regimes in turbulent premixed combustion.

Turbulent scales

In general, turbulence can be characterized as a three-dimensional, chaotic flow regime, which comprises a distribution of different-sized eddies. According to Reynolds, the propagation velocity v can be defined as the sum of mean velocity $\bar{v}$ and root-mean-square of the turbulent fluctuation v' as

$$v(x,y,z,t) = \bar{v}(x,y,z,t) + v'(x,y,z,t), \tag{2.15}$$

depending on space and time. The fluctuation v' can then be used to determine the turbulent kinetic energy k as

$$k = \frac{1}{2}\overline{v' \cdot v'}. \tag{2.16}$$

In many applications, turbulence can be idealized as homogeneous and isotropic. In these cases, the turbulent kinetic energy only depends on the axial component of velocity fluctuation u', which results in

$$k = \frac{3}{2}\overline{u'^2}. \tag{2.17}$$

Including this simplification, Kolmogorov formulated the eddy cascade hypothesis in 1941 [15]. It involves a steady transfer of kinetic energy k from large to

small scales, until the energy is finally consumed due to the viscous dissipation ϵ. This implies that the energy content depends on the characteristic size of the eddy, which is illustrated in Fig. 2.2. The graph relates the wavenumber $\bar{k}$ to the kinetic energy spectrum $E(\bar{k})$. $\bar{k}$ is defined as the inverse of the eddy size l_n,

$$\bar{k} = l_n^{-1}, \tag{2.18}$$

while $E(\bar{k})$ is the density of kinetic energy per unit wavenumber $\bar{k}$, which is proportional to dissipation and kinetic energy as

$$E(\bar{k}) \propto \varepsilon^{2/3} k^{-5/3}. \tag{2.19}$$

The two main scales are the integral length scale L, which contains most of the kinetic energy and the Kolmogorov length scale $\eta = (\frac{\nu^3}{\epsilon})^{1/4}$, where the energy is finally dissipated. The range between those scales is called inertial subrange, and follows the $k^{-5/3}$ law introduced in Eqn. 2.19. [23]

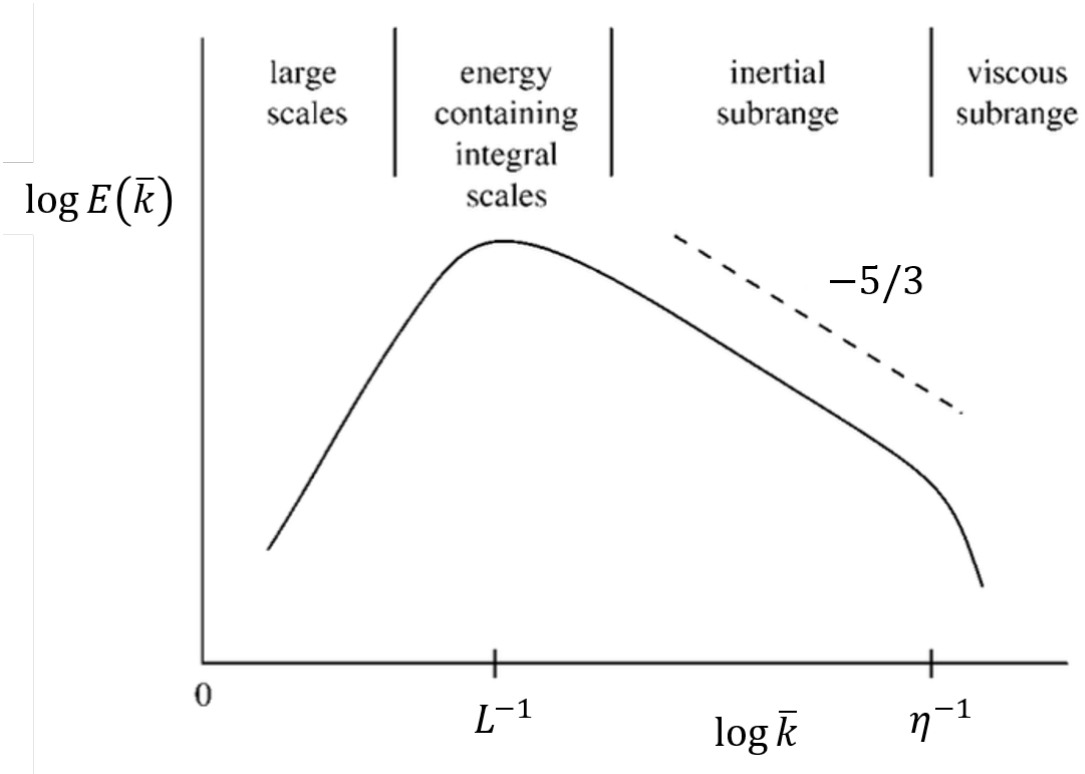

Figure 2.2: Turbulent kinetic energy spectrum [23]

Turbulent combustion regimes

The interaction of a turbulent flow field with a premixed flame results in the development of a turbulent flame. The random flow components deform the flame front, which leads to an irregular shape. In premixed turbulent combustion, various regimes can be formed. In order to describe these regimes, Borghi [5] proposed the diagram displayed in Fig. 2.3.

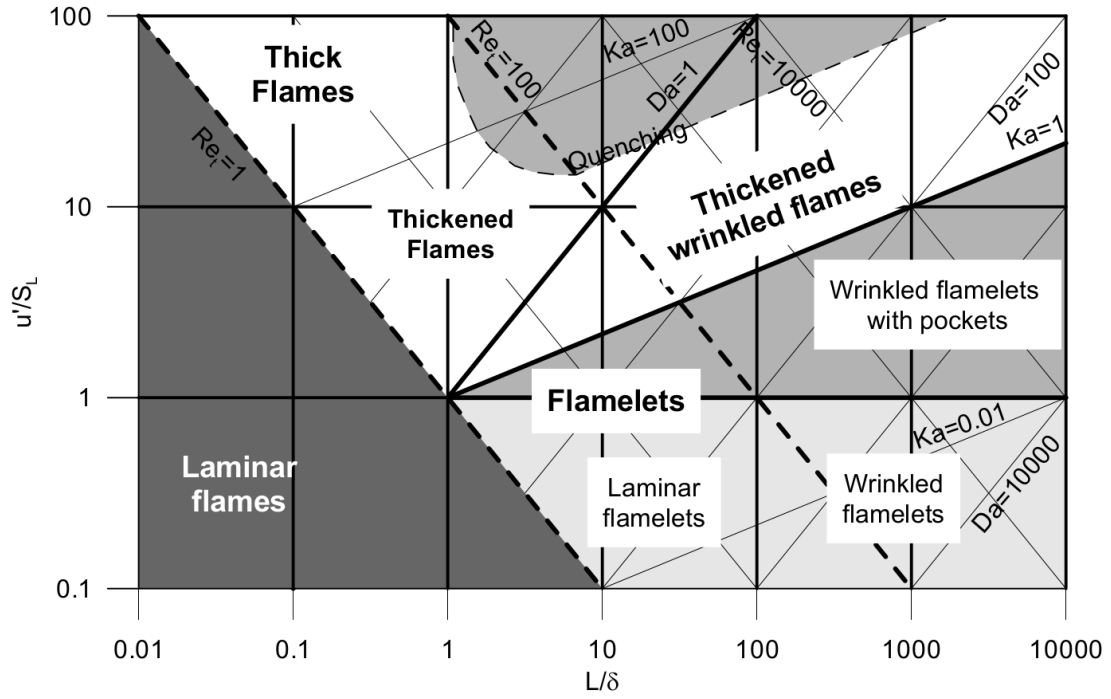

Figure 2.3: Regime diagram for premixed turbulent combustion [31]

The diagram axes show the logarithms of turbulent fluctuation u' and integral length scale L normalized against the laminar quantities S_L and δ, which is the laminar flame thickness

$$\delta = \frac{D}{S_L}, \tag{2.20}$$

where D denotes the molecular diffusivity. Different areas can be distinguished by comparing dimensionless numbers, such as the turbulent Reynolds number

$$Re_t = \frac{u'L}{S_L\delta} \approx \frac{u'L}{\nu}, \tag{2.21}$$

that relates turbulent inertial forces to viscous forces. The Damköhler number

$$Da = \frac{\tau_t}{\tau_L} = \frac{LS_L}{u'\delta} \tag{2.22}$$

compares the time scales of turbulent transport and the ones of laminar reaction. The Karlovitz number is defined as the ratio of laminar reaction time to Kolmogorov time scale as

$$Ka = \frac{\tau_L}{\tau_\eta} \text{ with } \tau_\eta = \sqrt{\frac{\nu}{\epsilon}} \text{ and } \tau_L = \frac{D}{S_L^2} = \frac{\delta}{S_L}. \tag{2.23}$$

The Kolmogorov scale means that the time an eddy of the size η needs for one turn is equal to the required time for diffusion through the eddy.

In Figure 2.3, different flame front types can be distinguished.
In the lower-left corner, the turbulent Reynolds number Re_t is below 1. In this case, the flame propagates in a *laminar regime*.
For Karlovitz numbers $Ka < 1$, the *flamelet regime* can be identified. In a flamelet, the smallest eddies are larger than the flame front thickness, which thus cannot be entered. This results in a quasi-laminar flame. Depending on the ratio of fluctuation to laminar flame speed $\frac{u'}{S_L}$, the flamelet area can be divided into two subregions.
For $\frac{u'}{S_L} < 1$, a *wrinkled flamelet* appears, that maintains a laminar inner structure. If the fluctuation u' exceeds the laminar flame speed S_L, the *wrinkled flamelet regime with pockets* is formed. Through the enhanced turbulence, individual parts (pockets) of the flame front can be separated. However, in spite of locally differing burning velocities, the flame remains in a quasi-laminar state. Due to the enlarged surface, flamelets burn at elevated burning speeds.
Within the range $1 < Ka < 100$, *thickened wrinkled flames* emerge. This regime is formed, if the flame front is penetrated by the smallest eddies. Accelerated turbulent transport leads to an increase in flame speed.
If the turbulent transport is further enhanced, *thickened flames* are formed. Due to the fast mixing of burned and unburned gas, the burning rate is mainly governed by reaction kinetics and not by mixing processes anymore.

2.4 Flame propagation mechanisms

Explosions can be described as the sudden release of energy. In combustion applications, the explosion event also includes a chemical reaction. If a flammable

mixture of fuel and oxidant is ignited, different flame propagation phenomena can occur. Deflagration and detonation represent the two main mechanisms, which show a different behavior regarding the resulting peak overpressure and pressure increase/decay rate.
Figure 2.4 illustrates the pressure history of these two combustion modes.

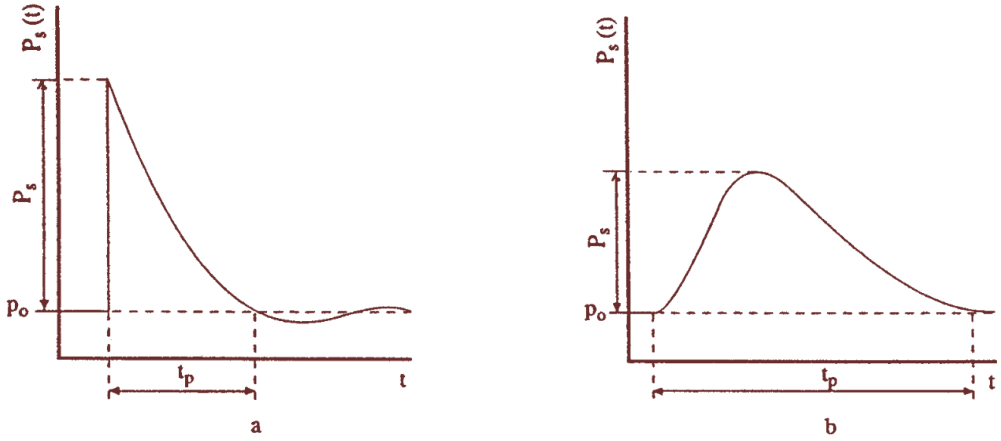

(a) Detonation **(b)** Deflagration

Figure 2.4: Pressure loads for different flame propagation mechanisms [13]

Deflagration

Deflagrations are chemical reactions that propagate at subsonic speed. The energy released during combustion is transported through relatively slow heat conduction and molecular diffusion processes. Even in more turbulent regimes, the reaction front cannot follow the pressure front, which moves at the speed of sound. As a function of flame speed, the pressure builds up gradually until the peak value is reached. Thereafter, the pressure starts to decrease. In total, this leads to a relatively long duration of the impulse[1]. In general, deflagrations are subdivided into slow and fast deflagrations. In the case of fast deflagrations, the flame front still propagates subsonically, while a shock wave is moving in the unburned mixture. However, the maximum temperature of the shock wave is still too low to ignite the mixture.

[1] time-integrated pressure

Deflagration to Detonation Transition (DDT)

DDT represents one possibility of detonation initiation. In this case, the transition between the two propagation mechanisms does not occur gradually, but rather instantaneously.

Detonation

Chemical reactions that move at supersonic speed are called detonations. The flame front is propagated by shock wave compression of the unburned gas. This shock can be seen in Fig. 2.4 (a). In contrast to a deflagration, the flame front and shock wave of a detonation proceed together. In the following reaction zone, the pressure drops to subatmospheric values, if the flame can expand freely. This results in the definition of a positive and negative phase. Apart from DDT, a detonation can also be induced directly by a significantly large source of energy, for instance an electric spark. In addition to that, Zel'dovich [32] discovered a detonation self-initiation mechanism, which is also known as SWACER (Shock Wave Amplification by Coherent Energy Release).

2.5 Flame acceleration

In section 2.4, different flame propagation mechanisms were presented. The regarded experiments yielded pressure loads generated by deflagrations. The intensity of pressure waves relates directly to flame velocity. While in section 2.3 various combustion regimes were displayed, this section focuses on the different factors that influence flame acceleration (FA). FA can depend on geometry, that is confinement or obstacles, flame instabilities and turbulence.

2.5.1 Role of instabilities

In the initial combustion phase, turbulence might not yet be completely developed. In this case, FA is predominantly influenced by flame instabilities. There

is a large variety of instability types, which includes Rayleigh-Taylor, Kelvin-Helmholtz, parametric and flame acoustic instabilities. In the transition phase from laminar to turbulent, Landau-Darrieus and thermodiffusive instabilities are expected to have a major impact.

Landau-Darrieus instability

Freely expanding flames are intrinsically unstable. This behavior can be attributed to the gasdynamic effects, which are related to the expansion of combustion products. Figure 2.5 shows a curved flame. In the burned gas, the streamlines converge and diverge behind the convex, respectively the concave part of the flame front. This results in additional curvature, thus enhancing the flame surface, which in turn causes an increase in flame speed. Experiments do not always exhibit this mechanism, as the instability might be damped by viscous or thermodiffusive effects.

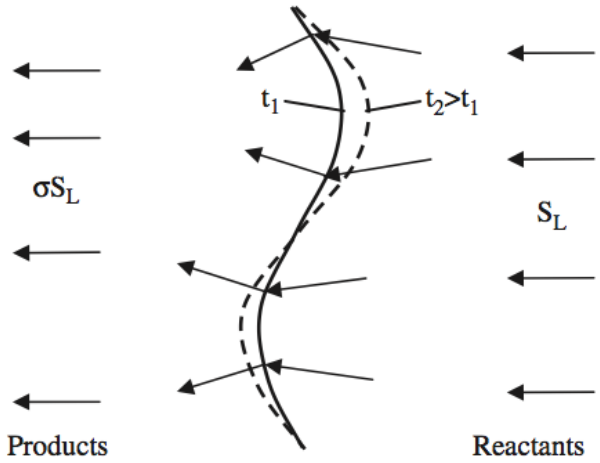

Figure 2.5: Schematic of Landau-Darrieus instability [8]

Thermodiffusive effects

The Lewis number describes the ratio of thermal diffusivity ($\alpha = \frac{k}{\rho c_p}$) to the molecular diffusivity of the limiting component D_L as

$$Le = \frac{\alpha}{D_L}. \tag{2.24}$$

Depending on the properties of the mixture (ϕ), the diffusivities might not be balanced. This entails the effects depicted in Fig. 2.6. For $Le < 1$, mass diffusion D_L exceeds diffusive heat flux α. Hereby, the local combustion temperature T_b is increased/decreased behind the convex/concave part of the front, which leads to locally enhanced/diminished burning velocities. For this reason, the flame is further wrinkled. In the case of $Le > 1$, the opposite effect can occur, that is a stabilization of the flame.

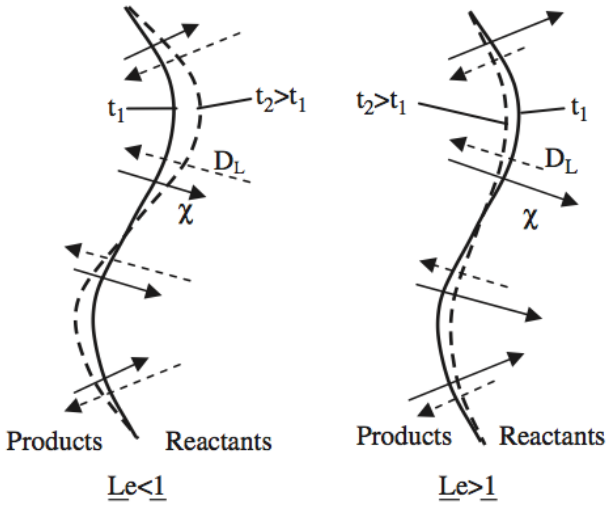

Figure 2.6: Schematic of thermodiffusive effects [8]

For the lean hydrogen-air mixture (15%; stoichiometric: 29.53%) considered in this work, $Le < 1$. Therefore, the effect of thermodiffusive instability (TDI) has to be taken into account. Figure 2.7 (a) shows that TDI leads to highly wrinkled, cellular flames. In Fig. 2.7 (b) ($Le > 3.8$), this effect cannot be observed.

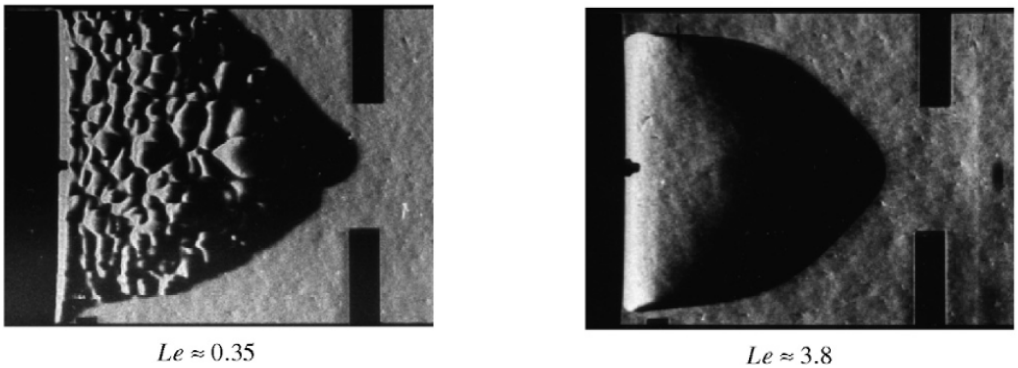

$Le \approx 0.35$ $Le \approx 3.8$

(a) 10% H_2 in air **(b)** 70% H_2 in air

Figure 2.7: Schlieren photos of initial stage of flame propagation [20]

2.5.2 FA through turbulence

Following a weak ignition, the flame usually remains laminar at the beginning. Through the emerging flame instabilities and the interaction with an increasingly turbulent flow field, transition to a turbulent regime takes place. Turbulence can enhance the local burning rate in two ways. Firstly, heat and mass transfer is increased. Secondly, enlarged flame surface can result in flame acceleration. However, increasing turbulence does not necessarily lead to higher burning rates. At high fluctuations, the flame can be stretched excessively and extinguished locally. As these quenching phenomena do not play a significant role in this thesis, they will not be detailed further.

The effect of wrinkling through turbulence in a duct is illustrated in Fig. 2.8. By comparing the mass flux $\dot{m}$ through the instantaneous turbulent flame surface area A_t with the flux through the cross-sectional area A, the relation

$$\frac{S_t}{S_L} = \frac{A_t}{A} = \Xi \tag{2.25}$$

follows. The flame speed is thereby enhanced by the wrinkling factor Ξ.

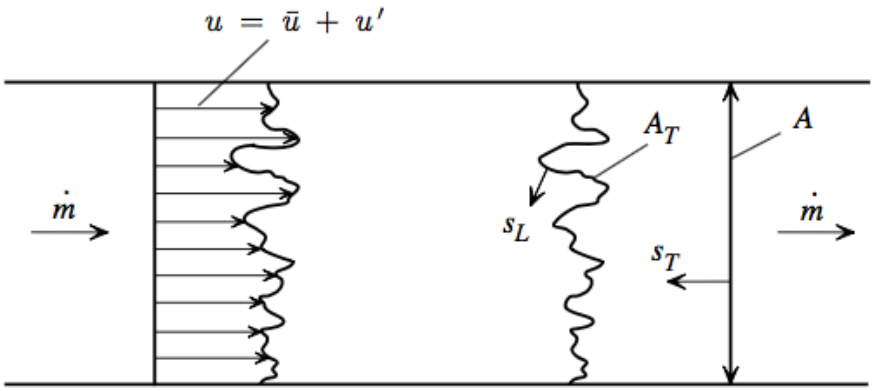

Figure 2.8: Idealized steady premixed flame in a duct [23]

The interaction of the flame with obstacles can be described as a positive feedback loop, which is displayed in Fig. 2.9. The combustion is followed by a pressure increase and subsequent expansion. The flow, which is pushed like a piston, interacts with obstacles. Additional turbulence is generated, thus further enhancing the combustion. If the explosion is not entirely confined, a second mechanism counteracts the feedback loop, which is called venting.

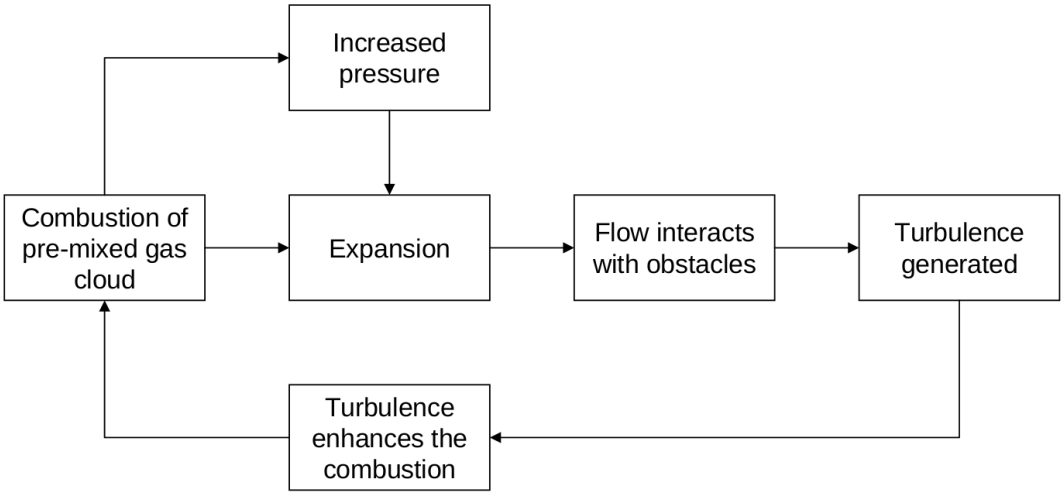

Figure 2.9: Feedback loop [31]

2.5.3 Explosion venting

Venting denotes a common safety measure to prevent exceedingly large pressure build-up caused by explosions inside enclosures. Certain international standards, such as EN 14994 [11] and NFPA 68 [22], give empirical correlations for the maximum reduced explosion pressure[2] $p_{red,max}$, derived in experiments with empty and relatively small vessels. In order to expand these guidelines to larger installations, Sommersel et al. [28] [29] and Skjold [27] performed experiments in 20-foot ISO containers.
By using pressure and flame speed measurements synchronized with high-speed videos, Bauwens et al. [2] [3] systematically investigated vented explosion cases similar to the scenarios regarded in the HySEA project. Hereby, up to three pressure peaks could be identified, which can be attributed to an external explosion (p_{ext}), flame-acoustic interactions as the flame approaches the container walls (p_{vib}), and a possible increase in flame surface area due to obstacles (p_{obs}). According to Molkov [21], an external explosion takes places if the dimensionless vent ratio meets the condition $A_V/V^{2/3} > 0.06$, whereas A_V and V denote the venting area and the free volume of the enclosure. This is the case for the deflagration venting scenarios considered in this work.

[2] $p_{red,max}$: "maximum pressure actually developed during a vented deflagration" [22]

3 HySEA project

3.1 Overview

The use of hydrogen, produced through electrolysis from renewable electricity, is one alternative to reduce the dependence on fossil fuels. However, its characteristic properties[1] call for certain safety measures. Progress in the field of hydrogen safety can be achieved both by experimental and numerical work. To this end, the EC Fuel Cell and Hydrogen Joint Undertaking initiated the HySEA (*Improving Hydrogen Safety for Energy Applications through pre-normative research on vented deflagrations*) project. The main objective is to provide experimental data for code validation and development.
The HySEA project consists of two large-scale experimental campaigns regarding different deflagration venting scenarios in homogeneous as well as inhomogeneous hydrogen-air mixtures with and without initial turbulence. The test program investigates a variety of parameters, such as mixture composition, vent area and the effect of obstacles within the container. Both campaigns include a blind-prediction study. This means that researchers and engineers can submit model predictions before the actual experiments are carried out. The hydrogen research group of IKET participated in the first of the two blind-prediction studies. In the following, the test set-up and experimental results will be presented.

3.2 Experimental set-up

For the first blind-prediction study, two different scenarios have been selected, as shown in Fig. 3.1: a 20-foot ISO container with open doors, with or without a bundle of 20 50-litre high-pressure gas bottles.

[1] Wide flammability range, very low ignition energy, high flame speeds

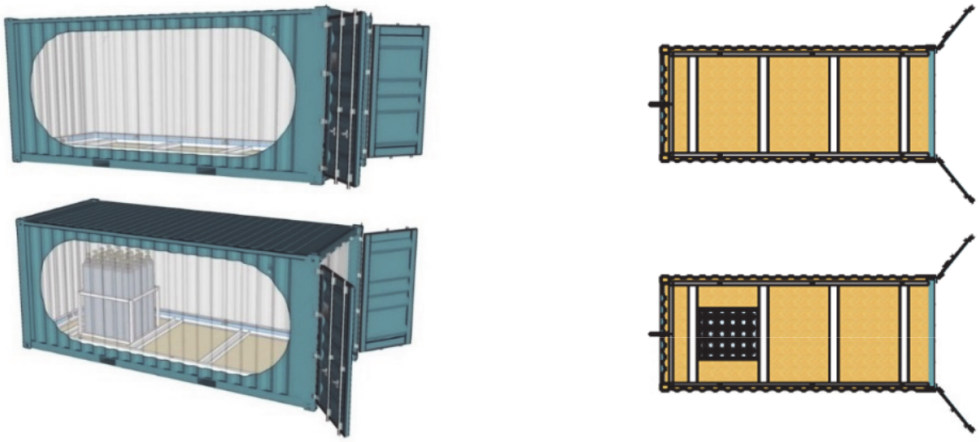

Figure 3.1: Set-up of the containers [27]

Figure 3.2 shows the dimensions of the container.

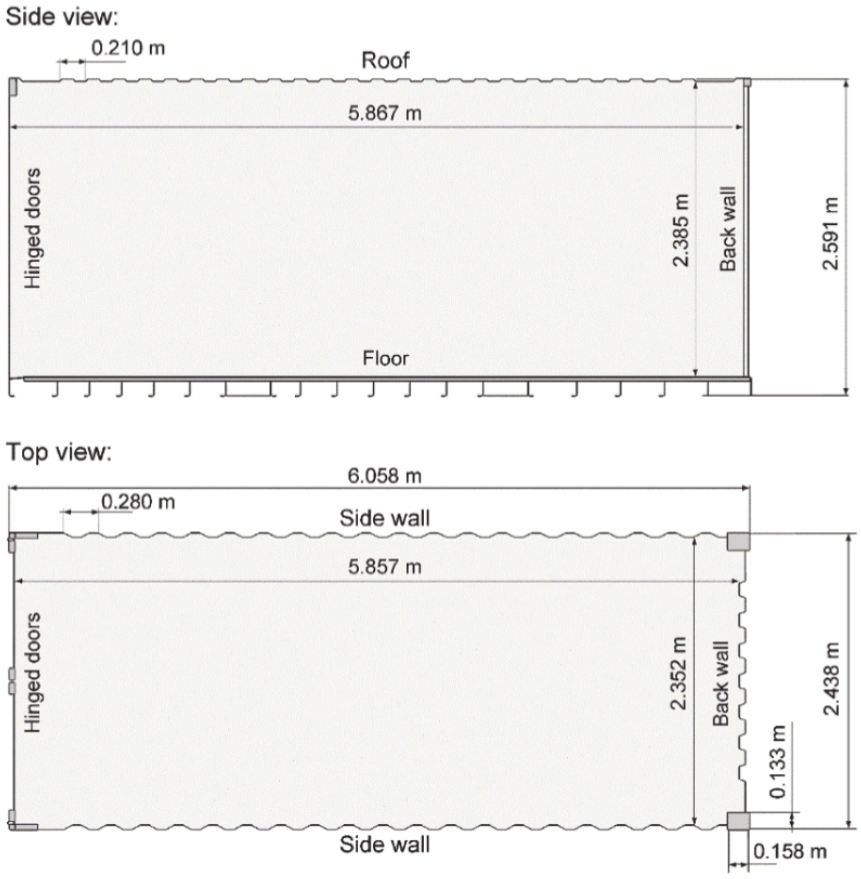

Figure 3.2: Dimensions of the container [27]

Within the container, a steel frame (Fig. 3.3 a)) is placed in order to protect eight pressure sensors (P01-P08) and signal cables. The frame consists of 200 mm x 75 mm U-beams and supports the bottle basket (Fig. 3.3 b)) in the second configuration.

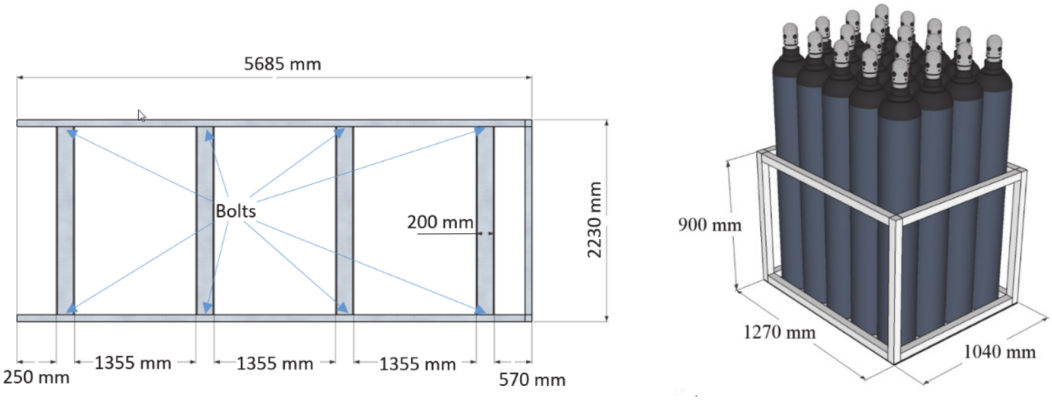

(a) Steel frame **(b)** Bottle basket

Figure 3.3: Frame and basket dimensions [27]

Due to a foundation constituted of two 360 mm H-beams, the container bottom is placed 0.36 m above the ground. By fixing the container to the foundation, movement during testing and thus damages to the measurement system are prevented. In Fig. 3.4, the experimental set-up prior to ignition is displayed. It can be seen that the opening is covered by a 0.2 mm polyethylene sheet, in order to keep the mixture within the container before ignition.

Figure 3.4: Open container doors, vent cover out of polyethylene sheet [27]

In both cases, a recirculation system ensures the homogeneous distribution of a lean hydrogen-air mixture. Prior to the ignition, the valves connecting recirculation system and container are closed to obtain a quiescent mixture and thus avoid initial turbulence. Ignition is initiated by an electric inductive spark discharge. Figure 3.5 indicates the location **A** of the spark plug at at the back wall of the container at mid-height. Moreover, eight internal (P01-P08) and three external (P09-P11) pressure transducers are installed. The deflection of the container walls (D1-D2) was also measured, but not considered in this work as it requires coupling the pressure load results from the CFD calculation with a finite element analysis simulation.

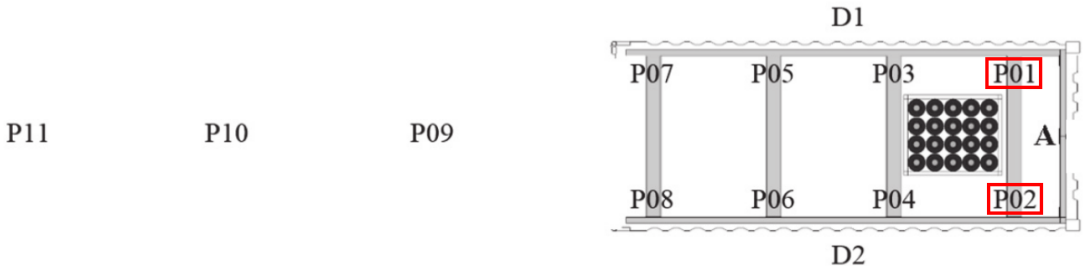

Figure 3.5: Pressure (P01-P11) and deflection (D1-D2) sensors, ignition location (A) [27]

Figure 3.6 shows the two experimental set-ups and the number of tests for each configuration. In the mixture, hydrogen amounts to 15 ± 0.2 $vol.\%$, yielding a fuel-to-air ratio of $\phi = 0.508$. By opening the doors, the vent area A_V equates to 5.64 m^2. The experiments are conducted approximately at atmospheric pressure.

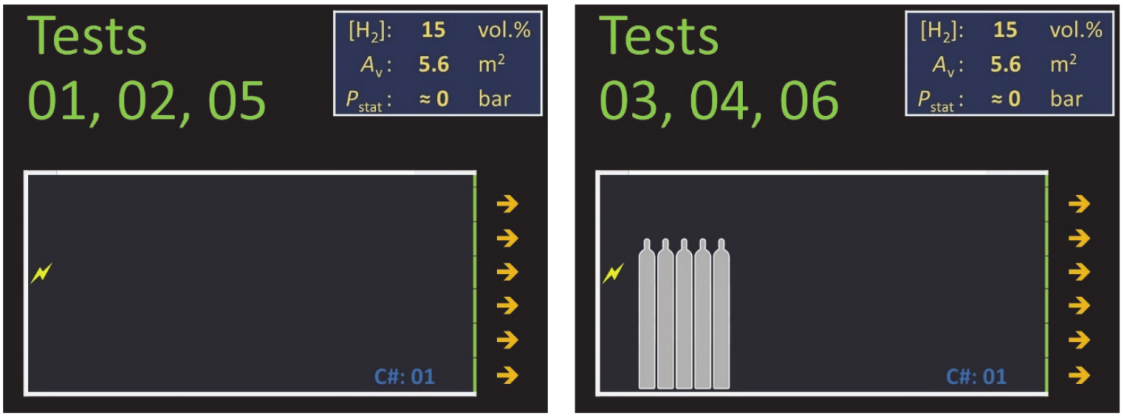

Figure 3.6: Both configurations of the test set-up [27]

3.3 Results of the blind-prediction study

Figure 3.7 lists the peak overpressure values at the individual transducers in *bar*. It becomes evident that the largest values, highlighted by bold font, occur at the sensors next to the ignition: P01 and P02. In addition to that, the remaining transducers (P03-P11) did, in some cases, not yield reliable results due to drift or noise. This refers to entries denoted with "NaN"[2]. As the focus of the performed simulations was laid on the initial combustion phase, chapter 6 only deals with the internal (P01-P08) and not the external pressure sensors (P09-P11).

Test	P01	P02	P03	P04	P05	P06	P07	P08	P09	P10	P11
1	0.039	**0.040**	0.026	0.031	0.018	0.021	NaN	0.015	0.007	0.004	0.002
2	0.045	**0.047**	NaN	NaN	0.039	0.031	NaN	0.023	0.012	0.005	0.003
5	**0.039**	0.038	NaN	NaN	NaN	NaN	NaN	NaN	NaN	0.002	0.001
3	0.075	**0.077**	NaN	NaN	0.064	NaN	0.033	0.040	0.024	0.012	0.009
4	0.062	**0.063**	NaN	NaN	0.058	0.064	NaN	NaN	0.014	0.007	0.005
6	**0.045**	0.044	0.039	0.034	NaN	NaN	NaN	NaN	0.013	0.016	0.004

Figure 3.7: HySEA maximum overpressure values [27]

Due to the observations above, the pressure sensors P01 and P02 are regarded more closely in the following. In Fig. 3.8, the pressure history of the tests without bottles is displayed. It has to be noted, that at such low overpressure values, the results are influenced considerably by noise. Therefore, the curves in Fig. 3.8 are already smoothed. Again, it can be seen that the transducers opposed to each other show strong similarities.
Apart from that, a certain variance between the tests can be detected. In terms of numbers, the largest overpressure in test 2 exceeds the corresponding maximum in test 5 by more than 20%. This discrepancy might be explained by drift and the uncertainty in mixture composition (15 ± 0.2 $vol\%$ H_2). Moreover, the six considered tests were performed within the same container, including possible damaging effects to the structure with each experiment.
In order to define a target area for the simulations, the maximum and minimum value at each moment is determined. This results in the boundary area, which is displayed in gray color in Fig. 3.9. For the configuration with bottles, the boundaries are also determined. Now, the experimental data can be properly compared to the results of the simulation.

[2]Not a Number

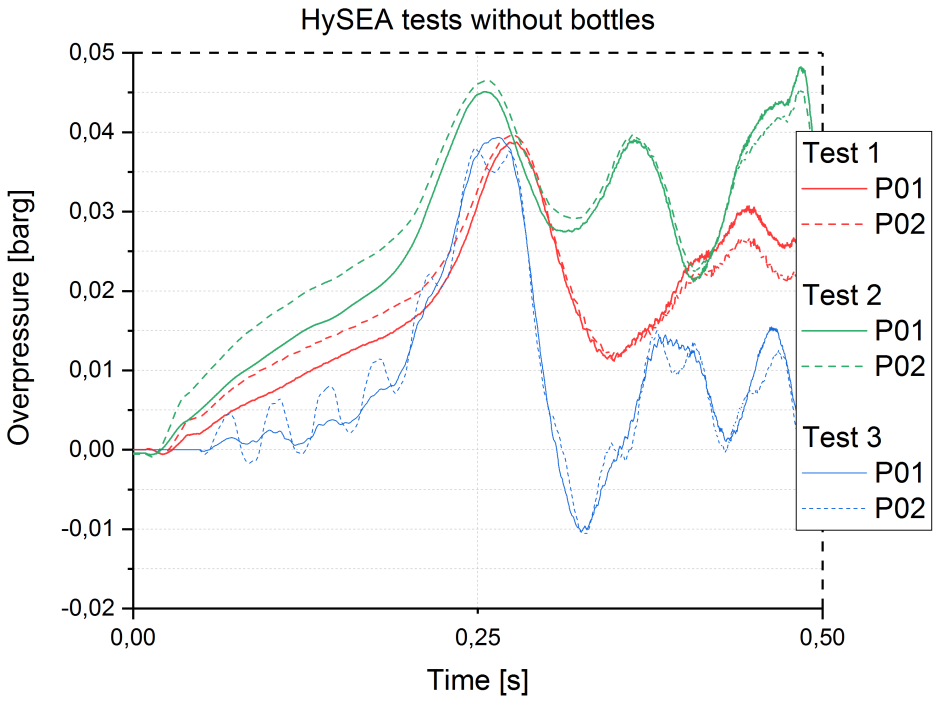

Figure 3.8: HySEA test results without bottles (test 01, 02 and 05) at P01-P02 [27]

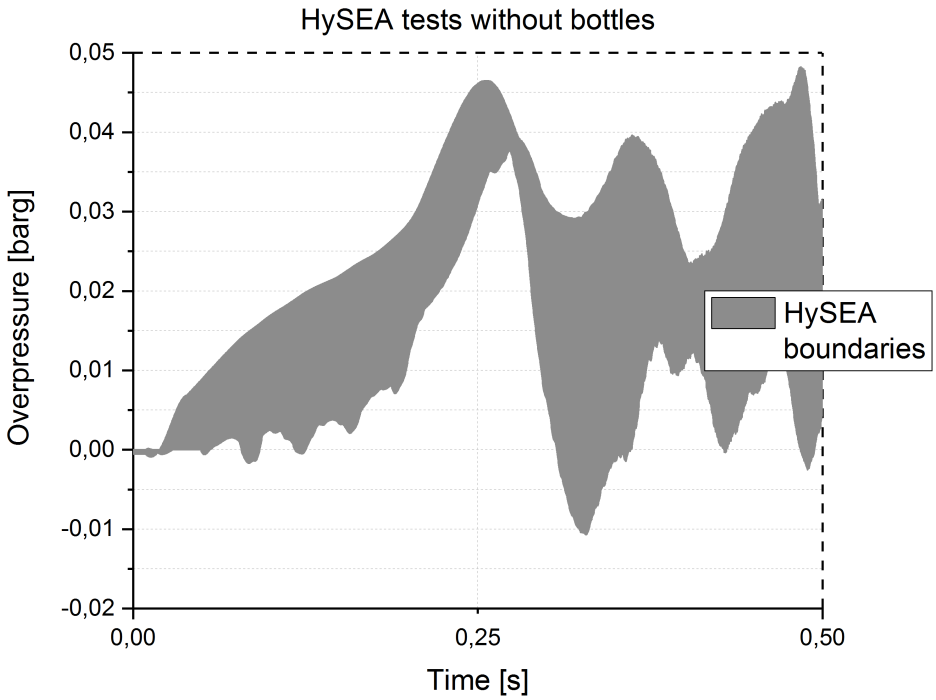

Figure 3.9: Boundaries of the HySEA tests without obstacle

Figures 3.10 and 3.11 depict the outcome of the model submitted by IKET for the blind-prediciton study without and with bottles. For both set-ups, the peak pressure values were significantly overestimated by a factor of about $1,8 - 3$. In particular the effect of the obstacle (Fig. 3.11) was overpredicted. Furthermore, the pressure peaks of the simulations are located too early in time, already in half the time measured.
In order to extend the meaningfulness of the simulation results, not only the location of the highest overpressure (P01-P02), but also the behavior of pressure over the distance to the back wall of the container is investigated. To this end, the lowest and highest peak overpressure values at each sensor position are selected. Figure 3.12 displays the experimental results of the internal[3] pressure sensors for the configuration without bottles, showing, once again, a relatively large discrepancy between the individual tests.

In conclusion, the model prediction produced an exceedingly violent combustion. Therefore, the results were considered to be not satisfying. This resulted in the idea of performing a post-blind calculation as the task of this work.

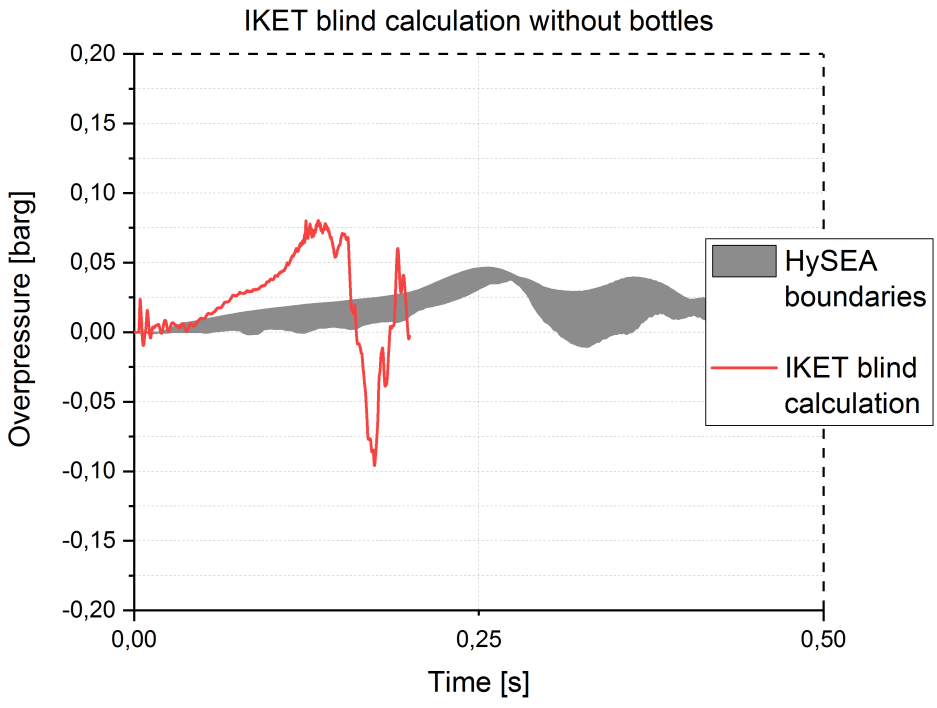

Figure 3.10: Blind-prediction results without bottles

[3]The solid line on the right side indicates the opening of the container.

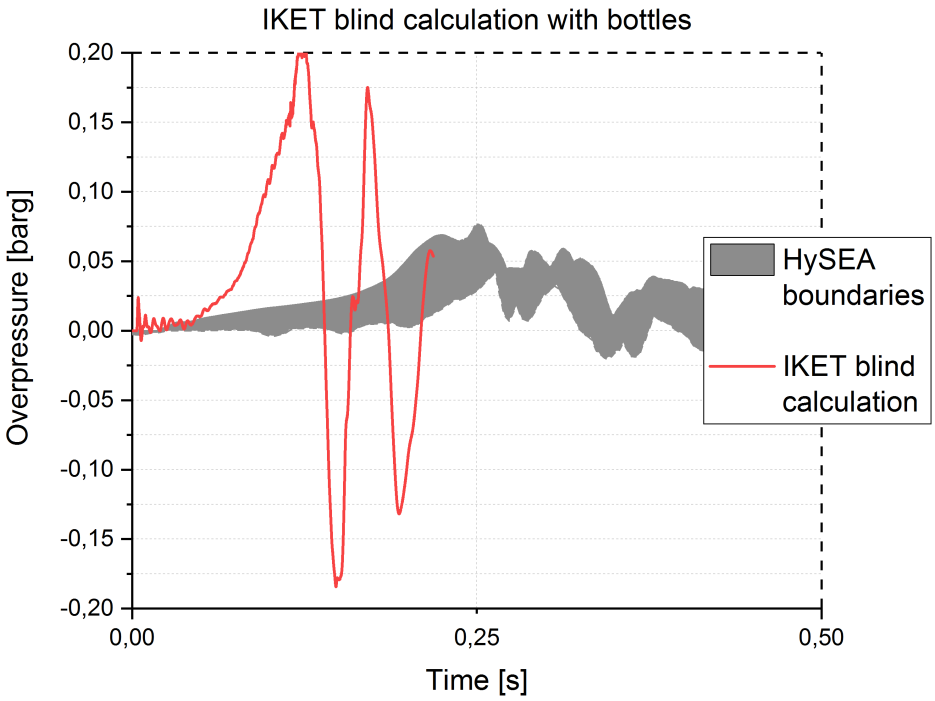

Figure 3.11: Blind-prediction results with bottles

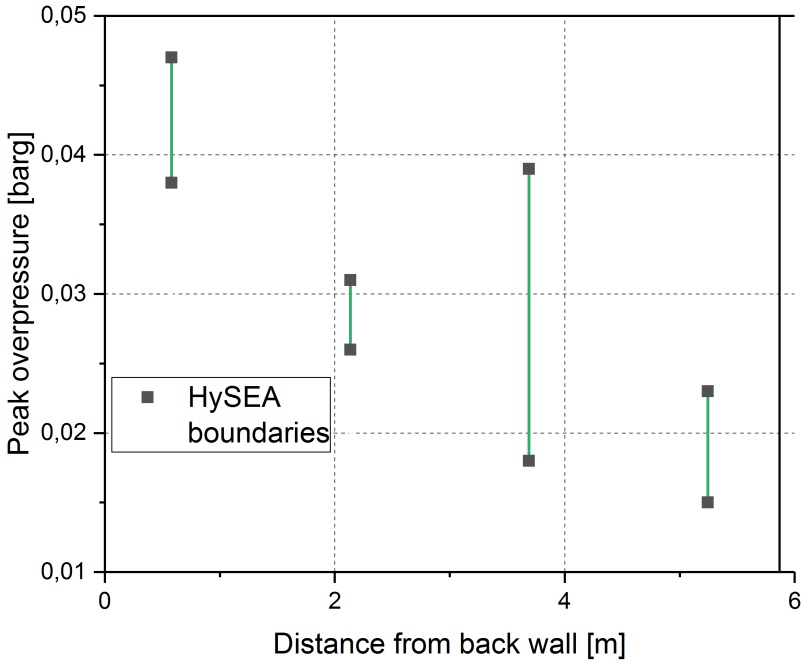

Figure 3.12: HySEA tests without bottles: Pressure vs. distance from back wall

4 COM3D combustion modeling

COM3D is a 3D code for turbulent reactive flow simulations, which focuses on the distribution and combustion of hydrogen. It is used to perform safety analyses for nuclear power plant accident scenarios and applications of hydrogen as an energy carrier. The quality of the results depends on a large variety of different models and parameters. The numerical solver and the turbulence model play an important role, and are already well established in the engineering community. In contrast, combustion and flame speed models, including the transition from laminar to turbulent combustion regime and the effect of instabilities, are under development. Therefore, this work focuses on the combustion model utilized most in COM3D: KYLCOM.

4.1 KYLCOM model

KYLCOM is a combustion model developed for COM3D. It belongs to the group of *turbulent flame speed* models[1] and consists of two parts. Firstly, the turbulent flame speed is determined. Then, the propagation of the flame is simulated.
Following certain phenomenological expressions derived in experiments, the turbulent flame speed S_t is related to different characteristic quantities of the flame. Highly sophisticated models include multiple parameters, which is illustrated in Eq. 4.1 as

$$S_t = f(\frac{u'}{S_L}, \frac{L}{\delta}, Le). \tag{4.1}$$

Amongst mentioned models, the formulation proposed by Schmid et al. [26] including the improvements made in [7] and [17] has proven its usefulness. However, in this work, another correlation developed by *Leeds University* is used, as it includes a multitude of factors and was validated extensively. In Eqn. 4.2, two different formulae are distinguished. Initially, only the expression S_{t2} was

[1] Alternatively, turbulent combustion can be modeled by considering the *structure of the flame*.

proposed [6]. However, it is only applicable to relatively high turbulence levels and thick flames, $KaLe < 38$, $Re_t/Le < 6000$. In order to account for moderate turbulence intensities, the correlation for S_{t1} was added by [14]. Adequate application of the formulae is achieved by selecting the minimum value of the two equations.

$$\begin{aligned} S_{t1} &= S_L \left(1 + 0.7 \left(\frac{u'}{S_L}\right)^{\frac{1}{2}} \left(\frac{L}{\delta}\right)^{\frac{1}{4}}\right) \\ S_{t2} &= 1.53\, u' \left(KaLe\right)^{-0.3} \\ S_t &= \min\left(S_{t1}, S_{t2}\right) \end{aligned} \tag{4.2}$$

The burning velocity serves as an input for the flame propagation, where KYLCOM offers two different models. The first option follows the *gradient model approach*[2] by [33]. Here, the purpose of the turbulent burning velocity S_t is to close the equation for the mean reaction rate as

$$\overline{\omega} = \rho_u S_t |\nabla \overline{f}|, \tag{4.3}$$

where ρ_u and $\overline{f}$ denote the density in the unburned mixture and the mean progress variable, respectively.
The second option, utilized in this work, follows the CREBCOM algorithm formulated by [10]. This method belongs to the category of forest fire models, which means that a cell starts burning as soon as one or multiple surrounding cells are consumed up to a certain limit. The progress variable f describes, how far the reaction is advanced. f assumes values between 0 for fresh mixtures and 1 for a completed reaction. In COM3D, the following burning criterion is applied:

$$F_{i,j,k} = f^2_{i+1,j,k} + f^2_{i-1,j,k} + f^2_{i,j+1,k} + f^2_{i,j-1,k} + f^2_{i,j,k+1} + f^2_{i,j,k-1} - 3f^2_{i,j,k}. \tag{4.4}$$

For $F > (\frac{1}{2})^2$, the cell is considered to be burning. This leads to the chemical reaction rate

$$\omega_{i,j,k} = \frac{df_{i,j,k}}{dt} = \frac{S_{i,j,k}}{\Delta}(1 - f_{i,j,k}), \tag{4.5}$$

with Δ as the cell size and S, which depends on the propagation speed and the expansion[3]. Otherwise, $\omega = 0$.

[2]The *level set approach* represents another modeling technique, which relies on a non-reactive variable, according to [23].
[3]For further explanation, see [31].

4.2 Original code structure

In COM3D, the user can choose between different combustion models. In all cases, the ignition is defined by the *forced combustion rate* H_K. Over the course of this work, the model KYLCOM was used in two different ways. The first option implies that the flame is propagated at a constant reaction rate, which requires only one input parameter, a fixed value for the fundamental turbulent flame speed S_t.
The alternative, enabling a more realistic view on the combustion phenomena, is to determine the turbulent flame speed locally. This procedure entails a large variety of parameters, which can be selected via the graphical user interface displayed in Fig. 4.1.

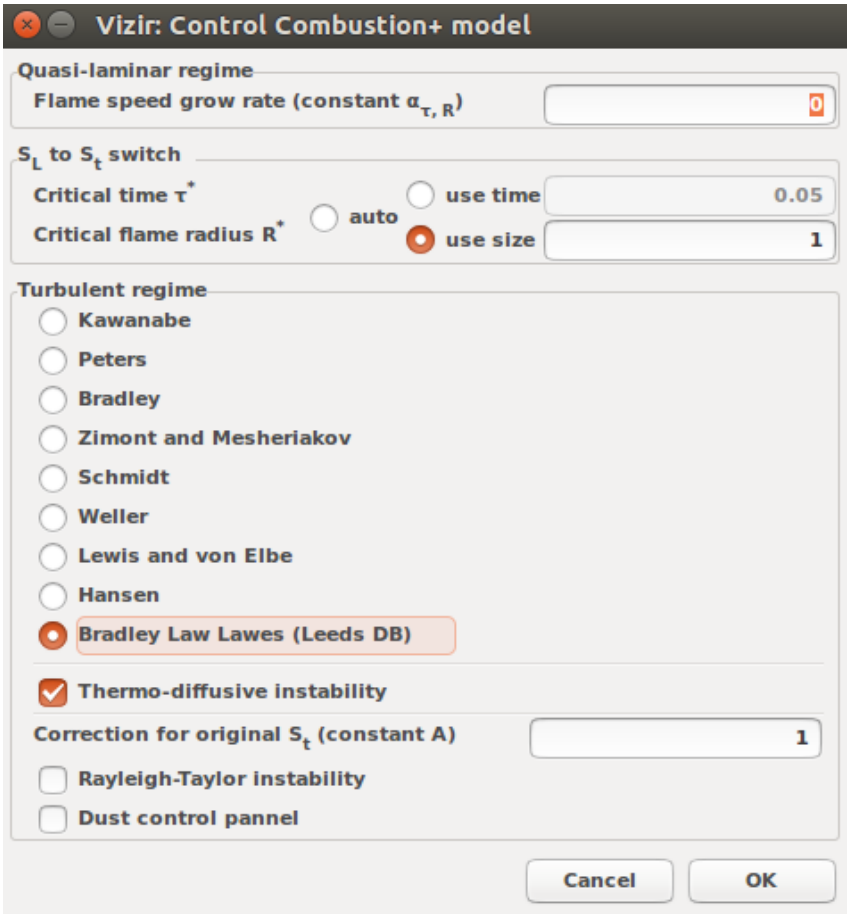

Figure 4.1: KYLCOM parameters

Combustion is usually initiated at laminar flame speeds. Thereafter, the flame

speed possibly grows before the turbulent regime is reached. This growth can be modeled as a quasi-laminar regime as

$$S_{ql} = S_L(1 + \alpha R)^{\frac{1}{2}}, \tag{4.6}$$

where S_{ql} denotes the quasi-laminar flame speed and R is the flame radius. By multiplying R with the constant α, a quasi-laminar regime is specified. In this work, α was set to zero, as quasi-laminar behavior can also be achieved by additional instability models.

After a certain distance, the flame proceeds in a turbulent regime. In reality, the transition takes places gradually, whereas in COM3D, the turbulent flame is developed instantaneously. The transition can be initiated by selecting a critical time or flame radius.

As soon as a turbulent flame is formed, a certain flame speed model is utilized. In this work, only the model by *Leeds University* was considered.

In section 2.5, the role of instabilities for flame acceleration was emphasized. If the effect thermodiffusive instability (TDI) shall be included, an effective Lewis number[4] Le_{eff} is calculated. For $Le_{eff} > 1$, no thermodiffusive effects are implemented. In contrast, for lean hydrogen-air mixtures, a constant flame wrinkling factor due to TDI Ξ_{TDI} is formulated following the simple model

$$\Xi_{TDI} = \frac{0.9}{Le_{eff}}. \tag{4.7}$$

Hereby, the exponent of -1 can be attributed to results by Driscoll [9]. The coefficient of 0.9 was added by Bauwens et al. [4] to further match Ξ_{TDI} to experimental data. Subsequently, Ξ_{TDI} is multiplied by flame speed, both for laminar and turbulent regime, resulting in the effective quantities

$$S_{L,eff} = \Xi_{TDI} S_L, \tag{4.8}$$

$$S_{t,eff} = \Xi_{TDI} S_t. \tag{4.9}$$

The COM3D code is also able to model Rayleigh-Taylor instability. However, it was not considered in this study, as an impact on the results was not expected. The reason was that the flame does not move upwards and the combustion takes places too quickly for this type of instability to play a role.

Another model option relevant to this work, is the possibility to define an effective fluctuation u'_{eff} by multiplying the fluctuation u' by a constant A as

$$u'_{eff} = A\ u', \tag{4.10}$$

an approach, which will be detailed further in section 5.4.

[4] In COM3D, Le_{eff} only depends on the equivalence ratio ϕ. More sophisticated approaches, e.g. as proposed by [25], also include turbulent characteristics.

4.3 Code modifications

In the course of this work, the importance of thermodiffusive instability (TDI) for flame acceleration was detected. This mechanism is considered by the TDI model described in the previous section. However, the turbulent flame speed model also implies flame wrinkling effects due to instabilities. In total, this leads to an overestimation of the pressure loads resulting from combustion, as in the case of the blind calculation in Fig. 3.10 in section 3.3. In order to allow blind-predictions in the future, this calls for model and code development.

In particular the early stages of combustion are mainly affected by instabilities. At such low turbulent intensities, the utilized flame speed model by Leeds University is not valid. This leads to the proposal of a code modification consisting of two parts:

- Change the criteria for the transition from laminar to turbulent regime
- Define a new TDI wrinkling factor Ξ_{TDI} with dynamic character

Transition from laminar to turbulent regime

The correlation 4.1 for the turbulent flame speed indicates that the turbulent flame speed model possibly already includes flame wrinkling. This results in the idea of applying the TDI model only to the laminar case. Consequently, the flame speeds for both regimes read

$$S_{L,eff} = \Xi_{TDI} S_L, \tag{4.11}$$

$$S_{t,eff} = S_t. \tag{4.12}$$

From the work of Bradley et al. [6], it can be concluded that their flame speed model approach is not valid for fluctuations below laminar flame speed. This leads to the assumption that the transition in the modified COM3D code takes place at

$$u' \approx S_L. \tag{4.13}$$

TDI model

In the current version of COM3D, the wrinkling factor due to TDI is assumed to be constant. The mixture composition considered in this thesis (15% hydrogen) yields a rather high value of $\Xi_{TDI} = 2.73$. Moreover, the instability is expected to be developed completely from the beginning, which results in a large influence by the TDI model.
However, the increase in flame surface provided by TDI does not happen at once, but gradually. According to Gostintsev et al., flame acceleration is sustained by the ongoing cell splitting, which generates fractal structures [12]. These self-similar patterns can be described by a power law, which expresses a dynamic character. Within the scope of their experimental research, Bauwens et al. attributed these effects to Darrieus-Landau instabilities [1]. As they investigated lean hydrogen-air mixtures, these effects are referred to as caused by TDI. After [1], the power law is defined as

$$\Xi_{TDI} = \frac{u_{eff}}{S_L} = (\frac{R}{R_0})^{\beta}, \tag{4.14}$$

where R_0 is the critical radius of the instability onset and β is the fractal excess. For the considered mixture, these two parameters are approximately $R_0 = 0.02\ m$ and $\beta = 0.24$.

Simulation procedure

According to the suggested modification, the flame changes from laminar to turbulent at around $u' = S_L$, which occurs at a critical transition distance $R_{transition}$. At the moment, $R_{transition}$ has to be determined manually by a preliminary calculation. After that, the actual simulation can be started. This procedure can be summarized in four steps, illustrated by Fig. 4.2:

- Step 1: Plot H_2 concentration isolines
- Step 2: Switch to turbulent kinetic energy k
- Step 3: Evaluate k, where already $\approx 10\%$ H_2 is consumed $\Rightarrow R_{transition}$
- Step 4: Start new simulation with determined $R_{transition}$

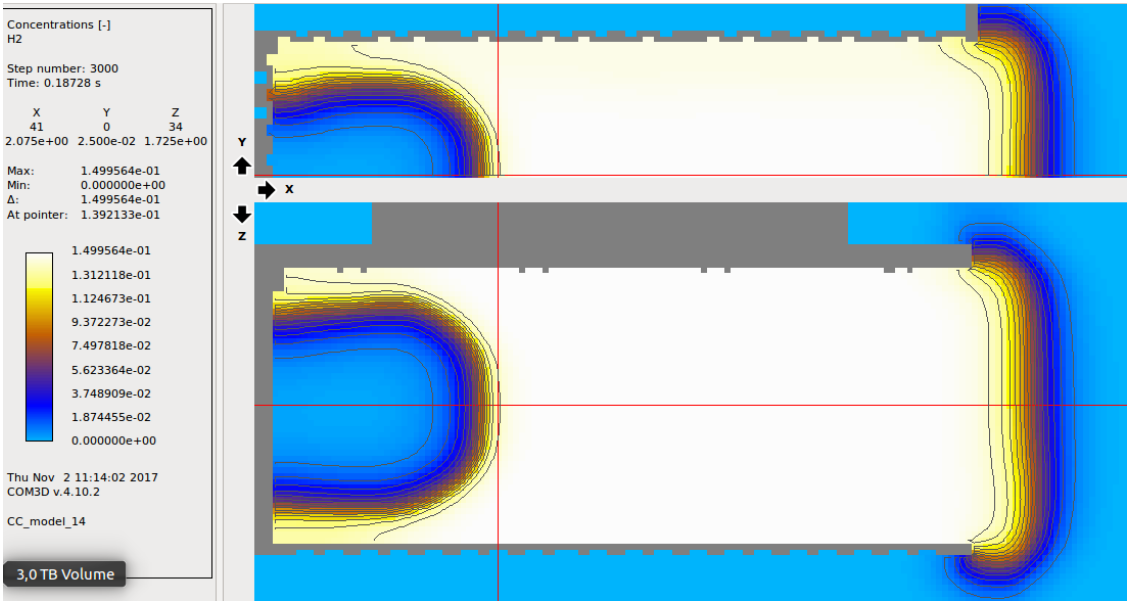

(a) Isolines H_2 concentration

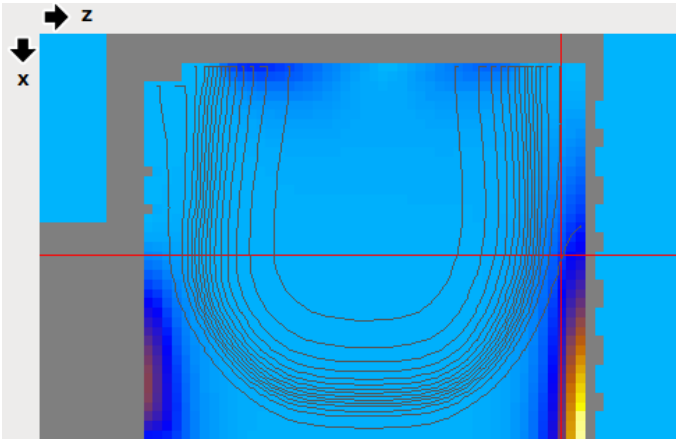

(b) Turbulent kinetic energy

Figure 4.2: Determination of $R_{transition}$

The current two-step simulation procedure was chosen to avoid massive coding, which would have been beyond the scope of this work. For the future, the idea is to automatically find and apply the transition criterion, rendering the preliminary simulation redundant.

5 Numerical simulation

A numerical simulation entails three rather independent steps:

1. Preprocessing
2. Calculation
3. Postprocessing

In the following, this procedure is detailed on the basis of the simulations performed in this work.

5.1 Preprocessing

Prior to the calculation, the problem has to be defined, starting with the geometry. In Fig. 5.1, the geometrical model of the container including three mounts for the external pressure transducers is displayed. The CAD model was created at IKET in advance of this work, in order to participate in the blind-prediction study.

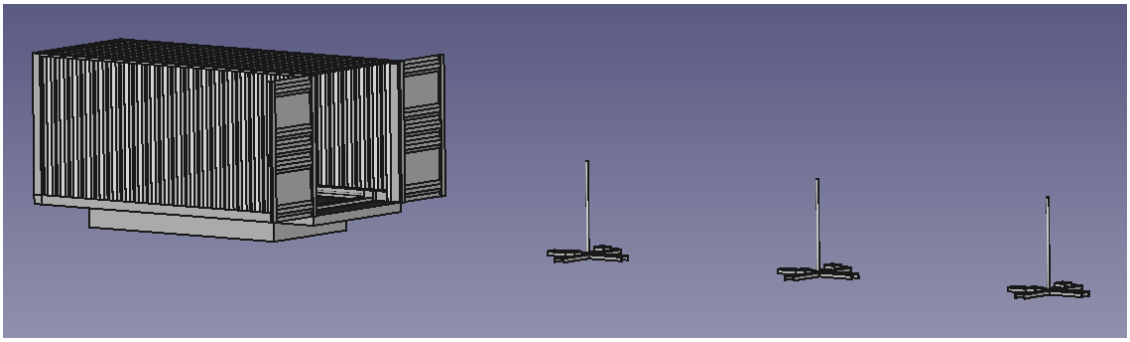

Figure 5.1: Geometrical model

After generating the geometry, the numerical model including an adequate mesh has to be deduced. To this end, the COMGEN routine is utilized through the following command:

```
>comgen -d 0.05 -x 0. -y 1.219 -z -0.36 -X 24. -Y 7.2 -Z 7. -f geometry.step
```

where the minus before a letter indicates an option. All the parameters related to dimensions are defined in meters, beginning with the cell size 'd'. For the majority of the simulations, 'd' was chosen to be 0.05 m, and 0.025 m for a refined version of the mesh to check for convergence. The lower-case characters 'x', 'y' and 'z' determine the origin of coordinates. The value 1.219 for the y-axis was chosen to only consider one half of the container. This follows a symmetry assumption due to the fact that opposing pressure sensors (e.g. P01 and P02, see section 3.3) yield almost identical values. In the geometry model, the origin lies on top of the steel frame. To include the frame, 'z' has to be set to -0.36. The upper-case letters denote the size of the domain in all three spatial directions. Finally, the option 'f' expects the input of a geometric model. Figure 5.2 shows the numerical model. For reasons of clarity, the mesh is not displayed.

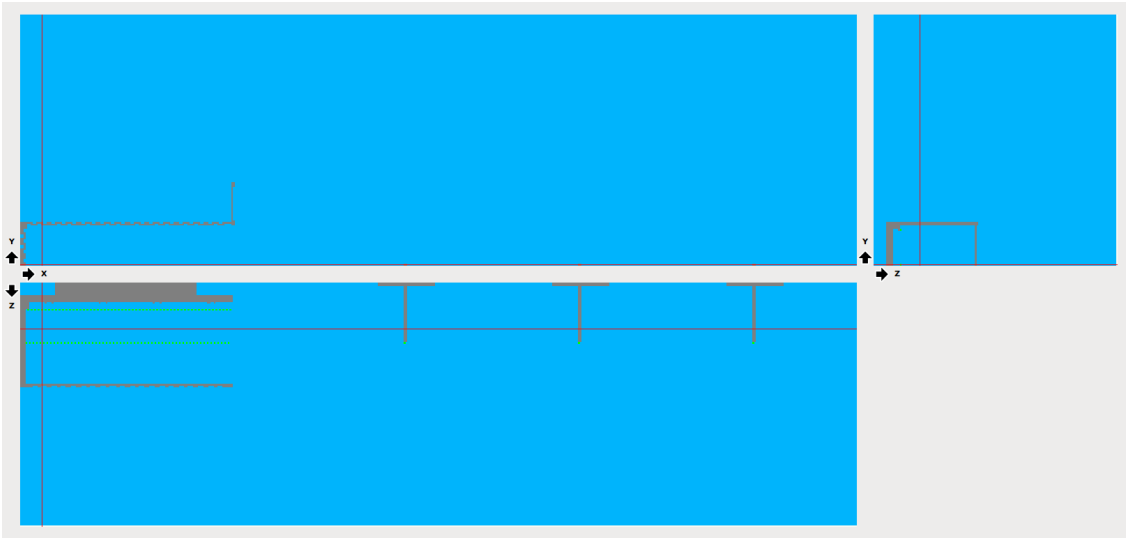

Figure 5.2: Computational model

After generating the mesh and saving the model to an '.nc' file, various conditions have to be prescribed. These informations have to be included in a '.geom' geometry file written in a 'pseudo-language'[1], as in Fig. 5.3.

[1]For further information, see [16].

The required parameters entail:

- Overall grid dimensions and grid cell size
- Regions with different gas properties
  - Initial temperature and pressure in each domain[2]
  - Starting values of turbulent kinetic energy k and dissipation ε
  - Position and size of the ignition
- Boundary conditions (BC), such as wall, mirror or open BC[3]
- Locations for gauges (for recording time-dependent information)

```
// CC_model_TDI_4

Dimensions:     480     144     140
Cell Size:      0.05
Unit:           Cell

// Ins01: Air
// Ins02: Air/Hydrogen
// Ins03: Air/Hydrogen --> Ignition

Rectangle:      Ins01   0 479     0 143     0 139
Rectangle:      Ins02   3 120     0  22    11  57
Sphere:         Ins03   3 0 34  2 2 2

// Boundary conditions

B_RX:   Open01  479    0  143    0  139
B_LY:   Mirror    0    0  479    0  139
B_RY:   Open01  143    0  479    0  139
B_RZ:   Open01  139    0  479    0  143


// Gauges

// Internal pressure gauges

Gauge:  6       20      15
Gauge:  11      20      15
Gauge:  16      20      15
```

Figure 5.3: Geometry file

[2]The properties are defined in a '.ini' initiation file.
[3]Some BC require an additional '.dat' file specifying the conditions outside of the domain.

Finally, COMFILE transforms the input data into a starting file named 'com000000.nc'[4], which can be read and interpreted by COM3D.

5.2 Calculation

For the calculation, three main components of COM3D work together:

- **com**: Main computational module receiving initial data from restart files[5]
- **vizir**: Graphical user interface (GUI) allowing to set parameters and view all physical properties in the calculation domain, also during a simulation
- **comserv**: Intermediate network server connecting **vizir** and **com**

For this work, the remainder of relevant parameters was selected with the aid of the vizir GUI. The exact configuration will be presented in section 5.4.

5.3 Postprocessing

After finishing a calculation, the results need to be processed. This can be done in multiple ways. In *vizir*, the restart files of type '.nc' can be opened, which helps to visualize various quantities, such as temperature, pressure, turbulent kinetic energy, etc. The COMPLOT routine enables to process the data recorded by gauges. For instance, the pressure history can be plotted at one or more locations. The information of multiple light transducers can be used to evaluate process dynamics, such as the visible flame speed over time or distance. In the course of this work, additional simple scripts written in Python were utilized to determine certain characteristics, such as the peak pressure value and the duration from ignition to the overpressure maximum.

[4]Command: >comfile -n model.nc -k model.geom -i model.ini.
[5]Starting from 'com000000.nc', where the number represents the time step number.

5.4 Container simulation

In the course of this work, a large variety of parameters[6] has been tested, resulting in an extensive simulation plan. As the focus was laid on combustion modeling, a few main approaches can be identified. Unless stated otherwise in chapter 6, the considered approaches share the parameter set[7] shown in Fig. 5.4. As solver, the most accurate option was chosen, a second order TVD Entropy solver. For performance reasons, the turbulence was implemented with a standard $k-\varepsilon$ RANS model. The combustion process is described by KYLCOM and the flame speed model by *University of Leeds*. In order to ensure rather quick ignition, thus minimizing calculation time, an ignition zone radius[8] 0.1 m was selected with a relatively high forced combustion rate[9] $H_K = 50$.

Parameter	Setting
Solver	Second order TVD Entropy
Turbulence model	Standard $k-\varepsilon$ RANS
CFL number	0.9
RED number	0.1
Natural parameters	Activated
Wall function	Activated
Combustion model	KYLCOM
Chemical equilibrium	Activated
Turbulent flame speed model	University of Leeds
Ignition zone radius	0.1 m
Forced combustion rate H_K	50

Figure 5.4: Parameter setting

Informations about flame speed, thermodiffusive instability and transition from laminar to turbulent regime are given in the next chapter.

[6] These include the numerical solver, ignition zone size and strength, domain size, type of boundary conditions, etc.
[7] Refer to the COM3D user's guide in [16] for further information on the parameters.
[8] Dimensions of the container for comparison: 5.87 m x 2.44 m x 2.59 m.
[9] Usually, $H_K \approx 1$.

6 Results and discussion

In this chapter, the pressure loads resulting from the post-blind simulations are presented and discussed. Due to the large amount of performed calculations, only the main approaches are considered. Thereby, the role of flame speed[1], thermodiffusive instability and transition from laminar to turbulent regime is investigated thoroughly.
The behavior of pressure is viewed as a function of both time (sensor closest to the ignition) and location (inside the container, depending on the distance to the back wall). In section 6.1, the results obtained with the original COM3D code are displayed. Subsequently, section 6.2 shows the results with the modified code. At the end, a comparison between the different approaches is drawn.

6.1 Original COM3D code

Regarding the post-blind simulation with the original COM3D code, five different approaches can be identified, which are displayed in Fig. 6.1. To clarify the role of individual mechanisms, flame speed and instability conditions are varied. Concretely, flame speed is assumed to be fixed, quasi-laminar or turbulent. In this context, thermodiffusive instability (TDI) is either switched on (+) or off (−). For the calculation, a radius R has to be chosen for the transition from laminar to turbulent regime.

[1] Note that in COM3D, the burning velocity is calculated with respect to the unburned fuel, which is also called fundamental flame speed. For convenience, the short term "flame speed" is utilized in the following. It is not be confused with visible flame speed, which describes the motion of the burned fuel.

Approach	Flame speed	TDI
Fixed fundamental flame speed	$S_t = 7\frac{m}{s}$	–
Quasi-laminar	$S_{L,eff} = \Xi_{TDI}\, S_L$	+
Turbulent case 1	$S_{t,eff} = \Xi_{TDI}\, f(u', \dots)$	+
Turbulent case 2	$S_t = f(u', \dots)$	–
Turbulent case 3	$S_t = f(Au', \dots)$	–

Figure 6.1: Approaches with the original COM3D code

6.1.1 Fixed flame speed

The first approach stems from the idea to perform a preliminary calculation to estimate the combustion conditions. In this case, the flame speed is not defined locally by phenomenological expressions and does not include thermodiffusive effects or a laminar-turbulent transition. In contrast, a constant flame speed is prescribed, approximated by means of the experimental data. This is based on the hypothesis that the pressure maximum is reached when the flame exits the container, which corresponds to the common idea of an external explosion pressure peak p_{ext} in vented deflagrations.
The container is $l \approx 6\ m$ in length. It takes $t_{peak} \approx 0.2 - 0.25\ s$ until the first pressure peak[2]. This results in a flame front velocity of $v_b = \frac{l}{t_{peak}} = 24 - 30\ \frac{m}{s}$. Assuming an expansion ratio of $\phi = \frac{\rho_u}{\rho_b} \approx 4$, the fundamental burning velocity is given by $v_u = \frac{v_b}{\sigma} \approx 6 - 7\ \frac{m}{s}$, which serves as main input for the calculation. After some model tuning, the flame speed was determined as $S_t = 7\ \frac{m}{s}$.
Figure 6.2 shows the resulting pressure history in red, compared to the boundaries of the HySEA experiments in grey. The ignition is delayed by around 0.25 s. After ignition, the pressure gradient shows a similar behavior, leading to a fitting period between ignition and pressure peak. Most importantly, the peak pressure of the simulation is in good agreement with the experiments. Figure 6.3 illustrates that the simulation correctly reproduces the tendency of decreasing overpressure maxima over distance. In conclusion, this proves to be a valid approach to estimate combustion behavior. For better predictability, however, KYLCOM has to be utilized.

[2] As a reference for categorizing t_{peak}: the speed of sound in the given hydrogen-air mixture amounts to 380 $\frac{m}{s}$, meaning that pressure waves need, starting from the ignition point, about 0.003 s to reach the side walls (distance: 1.2 m) and 0.015 s until the container exit.

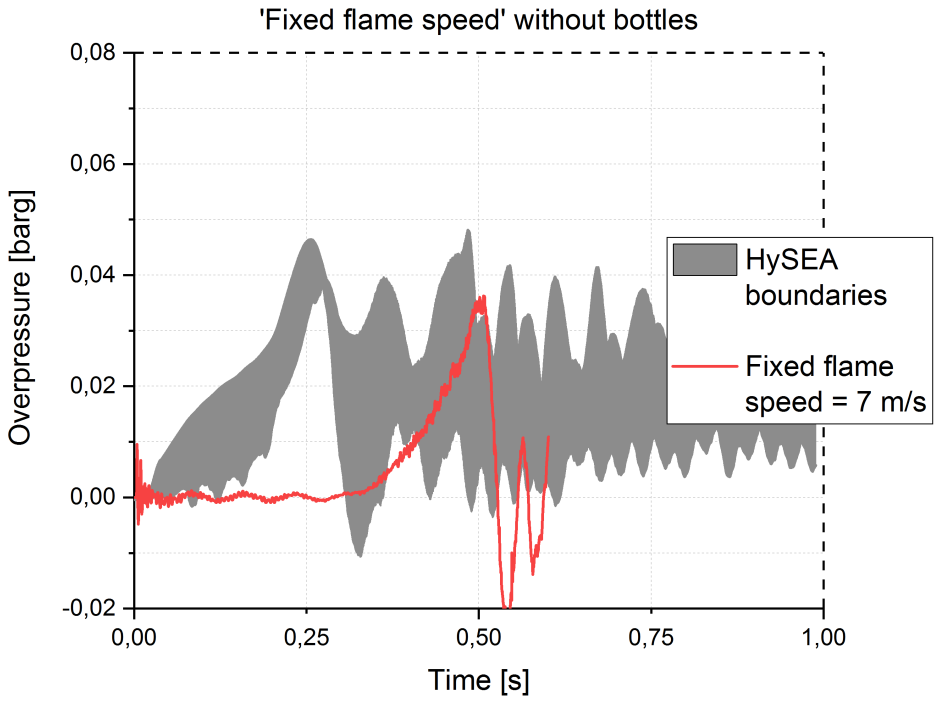

Figure 6.2: Fixed flame speed: pressure vs. time

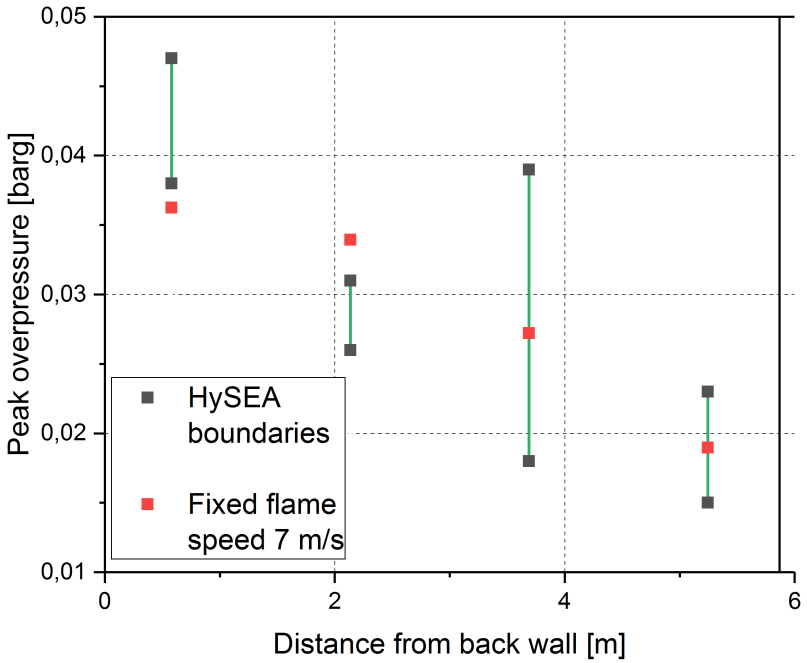

Figure 6.3: Fixed flame speed: pressure vs. back wall distance

6.1.2 Quasi-laminar regime

Apart from the role of instabilities in flame acceleration, the transition to turbulence is provoked by the interaction with obstacles and confinement. As the test set-up without bottles does not contain obstacles, a quasi-laminar regime might occur. Concretely, a laminar flame is assumed including wrinkling effects by instabilities. According to [24], laminar flame propagation in elongated, closed or half-open (at the opposite end of ignition) combustion chambers possibly leads to the formation of a flame front with inverted curvature, also called tulip flame or, in a previous state, finger flame. For the simulation, this approach implies that the regime remains laminar until a distance of $R = 6\ m$ is reached, marking the end of the container, while flame acceleration is provided by activating the TDI model.

Figure 6.4 shows that this approach yields a suitable pressure peak value. Directly after ignition, relatively strong oscillations can be observed. This is caused mostly by choosing a large value for the forced combustion rate $H_K = 50$, which ensures a rapid ignition. Hereby, computing power is saved. This approach is justifiable as the impact of H_K on the maximum pressure proved to be negligible. This effect also occurs in the following simulations.
Rather quickly after ignition, in about two thirds of the expected time, the first pressure maximum is reached. Therefore, the impulse of the experiment is not reproduced entirely satisfactory. This does not only apply to the first pressure peak but to the pressure curve as a whole, which exhibits an enlarged frequency. This could be explained by the interaction with the walls, which are simulated as rigid bodies. In contrast, the walls in reality are able to dampen the explosion pressures.
Figure 6.5 confirms the expected trend of pressure over distance. Still, the peak overpressure does not decline as quickly as in the experiment.
Nevertheless, this approach can be considered successful for this special configuration, as the global maximum pressure value is assessed correctly.
However, solely quasi-laminar behavior contradicts the common assumption by Lipatnikov [19], which expects a transition to turbulent regimes at around one meter. Therefore, the remaining simulations focus on predominantly turbulent flames.

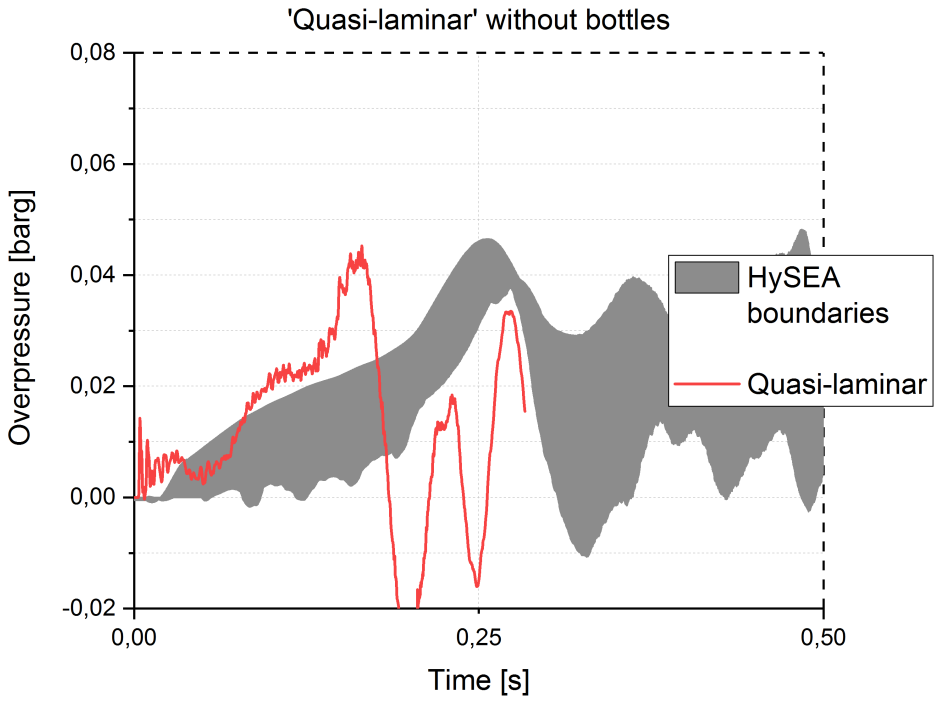

Figure 6.4: Quasi-laminar: pressure vs. time

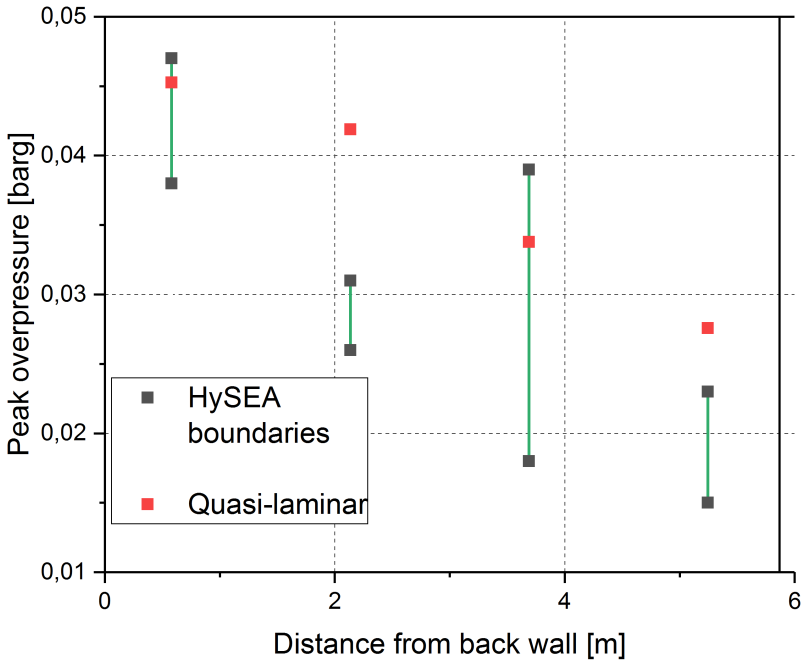

Figure 6.5: Quasi-laminar: pressure vs. back wall distance

6.1.3 Turbulent cases

Despite the absence of obstacles in the first experimental set-up, turbulence can be generated, e.g. by the interaction with the walls. Therefore, several turbulent cases are investigated. Hereby, the roles of the turbulent flame speed model ($S_t = f(u', ...)$) with a focus on the most important turbulent quantity, the fluctuation u', and the TDI model are reviewed closely.

Case 1: 'Turbulent TDI+'

The first case corresponds roughly to the assumptions made for the blind-prediction study, meaning that after one meter, the flame propagates in a turbulent regime, while taking thermodiffusive instability into account. Figure 6.6 illustrates that these settings result in overpressure values, which are significantly too large. This can be explained by having a look on flame wrinkling, as both flame speed model (FSM) and TDI model contribute to flame wrinkling with a respective factor Ξ_{FSM} and Ξ_{TDI}. Moreover, the characteristic of the curve differs, as multiple peaks and a continuous increase in pressure at the end can be identified. This might be due to enhanced reflections at the boundaries of the domain, which were partly closed for this simulation.

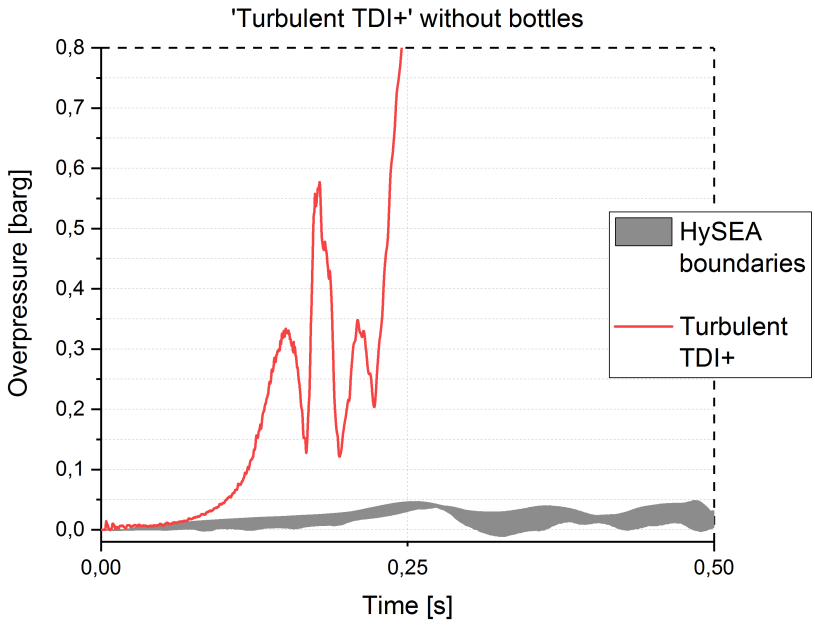

Figure 6.6: Turbulent TDI+: pressure vs. time

Case 2: 'Turbulent TDI-'

Due to the exceedingly elevated overpressure in case 1, the TDI model was deactivated in case 2, while the transition to turbulent regime was expected directly after ignition[3]. In this case, illustrated in Fig. 6.7, the pressure increase does not take place until 0.5 s and yields an underpredicted maximum value by a factor of $2-3$. A possible explanation is that flame wrinkling effects are only represented by the FSM, Ξ_{FSM}, which is not sufficient to model the entire extent of flame acceleration.

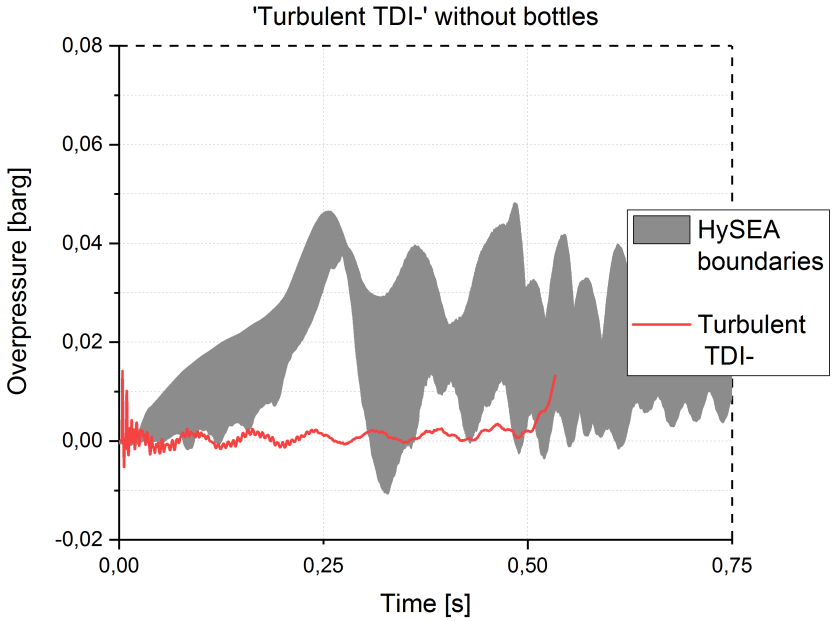

Figure 6.7: Turbulent TDI-: pressure vs. time

The first two turbulent cases show that for such low-turbulence applications, instability has a major impact on results. Neither with nor without TDI, the experiment was matched. However, there is a third option.

[3]Radius $R = 0$.

Case 3: 'Artificial instability'

Deactivating the TDI model results in overly reduced pressures. This problem can be avoided by making use of the parameter A mentioned in section 4.2. As a reminder, A enhances the turbulent fluctuation to an artificial effective value $u'_{eff} = Au'$. The idea behind this approach is that artificially enlarged turbulence results in further flame acceleration, thereby mimicking the effect of instabilities. Mathematically, this means that the total flame wrinkling is provided by the flame speed model as $\Xi_{FSM} = \Xi_{total}$. For the considered scenarios, the turbulence enhancing factor was tuned to a value of $A = 4$.

Figure 6.8 illustrates the results of two calculations without bottles, one for the normally assumed cell size of 5 *cm* (red curve) and another refined version with a cell size of 2.5 *cm* (blue curve). In both simulations, the pressure peak value lies within the boundaries given by the experiments. The pressure history presents a very good location in time, which implies ignition right at the start as well as a good match of pressure impulse. Furthermore, the oscillations after the main peak, which are mostly due to flame-acoustic interactions[4], can be detected clearly, again with an increased frequency possibly due to the added stiffness of the walls. The utilization of two different mesh sizes indicates that the model shows convergence for the selected parameter set, as the refined version approaches the experimental results. Actually proving convergence would require another mesh refinement.
In particular the initial pressure gradient including peak overpressure shows very good agreement with the experiments. In comparison to the coarse model, the refined mesh yields a slightly higher peak value. This behavior is reasonable due to the enlarged numerically modeled flame surface, which allows enhanced fuel consumption and thus increased flame speed. The advanced location in time compared to the coarse mesh can be attributed to the same mechanism[5]. Whereas in this case, the coarse model shows a small delay of pressure peak, the refined simulation is very accurate in time.
Figure 6.9 shows that the tendency of pressure over back wall distance is reproduced correctly, whereas, again, the gradient is not large enough. However, the largest peak overpressure lies accurately within the interval determined by the experiments.

[4]See p_{vib} in section 2.5.3.

[5]Ideally, physical quantities should not be coupled to discretization. However, limited computational performance does not always allow for satisfyingly resolved combustion simulations.

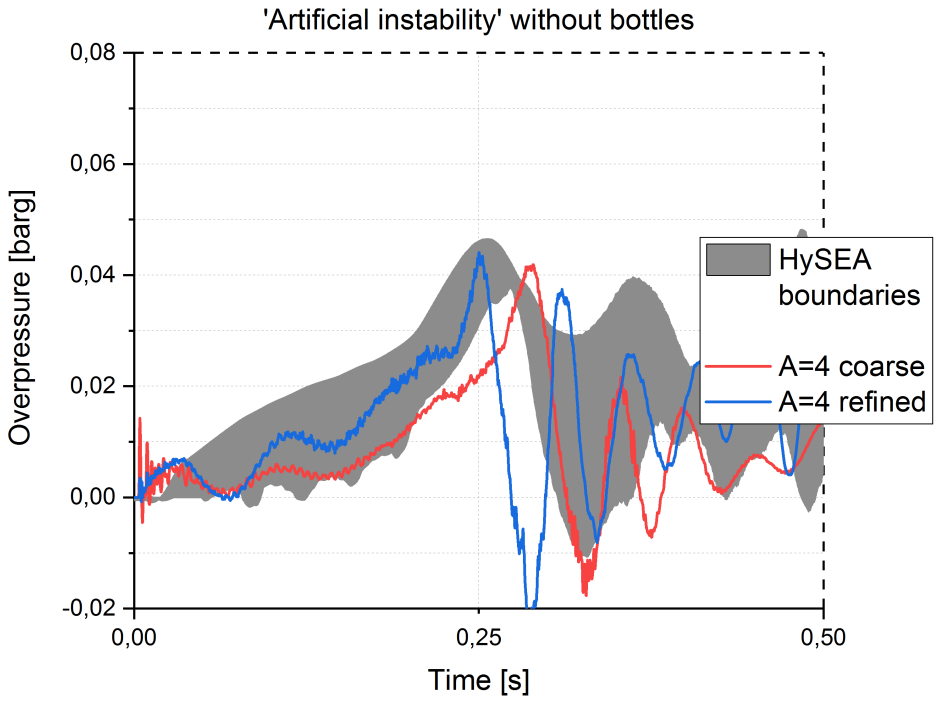

Figure 6.8: 'Artificial instability' without bottles: pressure vs. time

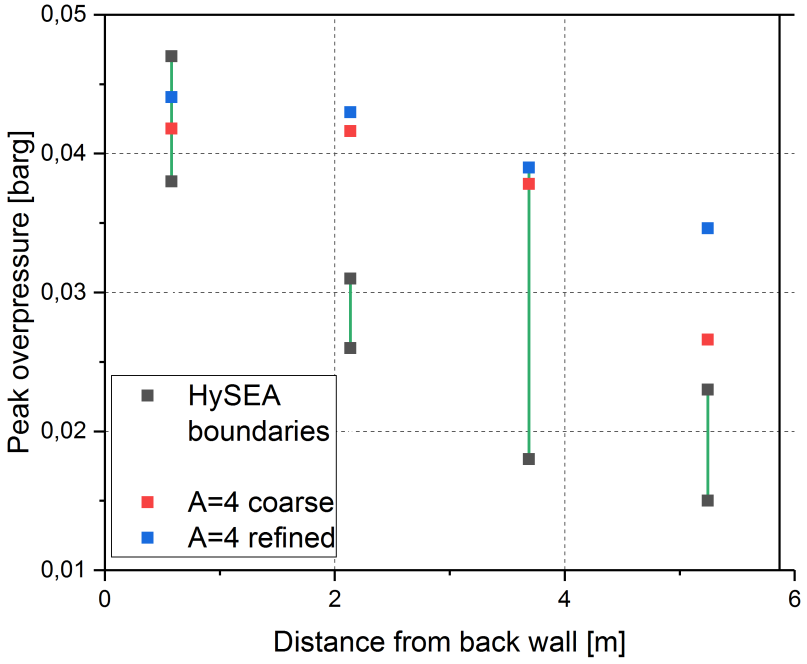

Figure 6.9: 'Artificial instability' without bottles: pressure vs. back wall distance

As this approach proved to be successful for the configuration without bottles, the same parameter set was utilized to simulate the set-up with obstacles.

The results are displayed in Fig. 6.10. Again, the pressure peak value is reproduced accurately. In contrast to Fig. 6.8, both mesh configurations reach the pressure peak before the moment measured in the experiments, leading to an underestimated pressure impulse. Furthermore, the HySEA boundaries depict a certain double-peak characteristic, which is not captured by the simulation. A comparison between coarse and refined mesh shows a similar, but more pronounced constellation as for the set-up without bottles. Specifically, the discrepancy of the peak values is more significant. This might be explained by geometric effects, meaning that the coarse mesh does not include a sufficient amount of detail of the bottle basket. This could also be a reason for the absence of the mentioned double-peak feature, which can be identified, if at all, in the refined version. Nevertheless, the double-peak could also be caused by deficient measurement. Further tuning in the sense of adjusting the parameter A would probably not improve the results. By increasing A, a larger overpressure maximum would be obtained with the side-effect of having an even more advanced location in time. In the opposite case, decreasing A yields a better location of the pressure in time, which in turn results in an overly low peak pressure. Therefore, no further tuning was performed, particularly due to the accurate reproduction of the main quantity, pressure.
In contrast to the calculations before, the simulation with bottles did not reproduce the pressure vs. distance curve correctly. In Fig. 6.11, the HySEA tests do not exhibit the continuous pressure drop observed before. Precisely, after a reduction in peak overpressure from the first to the second transducer position, the third sensor measures an increase, before pressure decreases again at the fourth position. In the simulation, the opposite effect occurs, meaning that the second transducer measures the largest peak overpressure, which contradicts expectation and experiments. Hereby, it remains questionable, if further mesh refinement would yield a more satisfactory result. Still, it has to be noted that the simulated overpressure at position two does not exceed the measured overall maximum value (at position one), which is the most important result for assessing the safety of the considered explosion scenario.

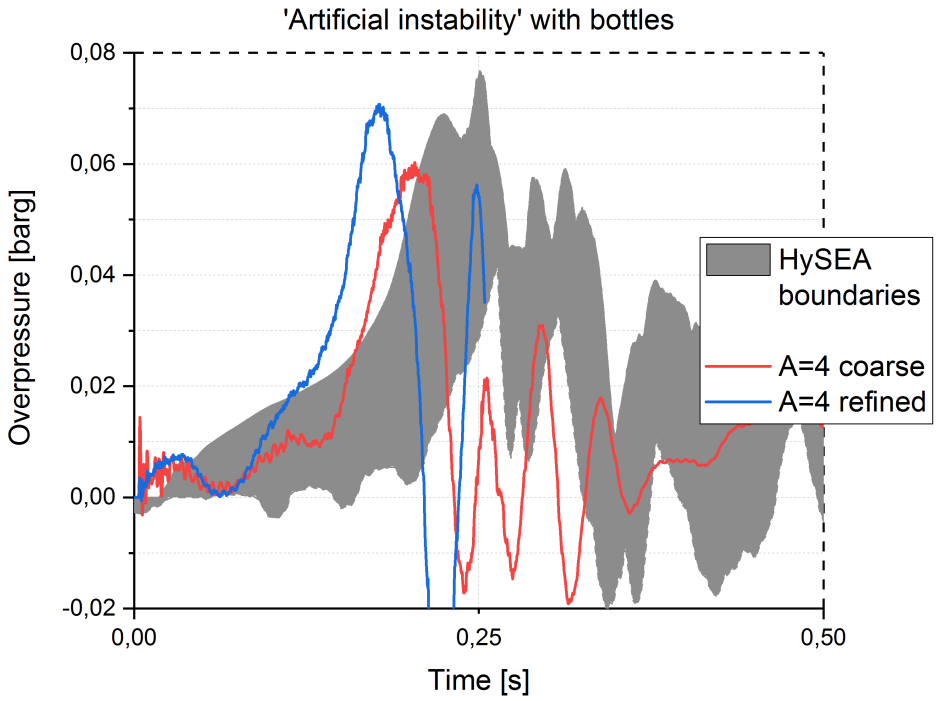

Figure 6.10: 'Artificial instability' with bottles: pressure vs. time

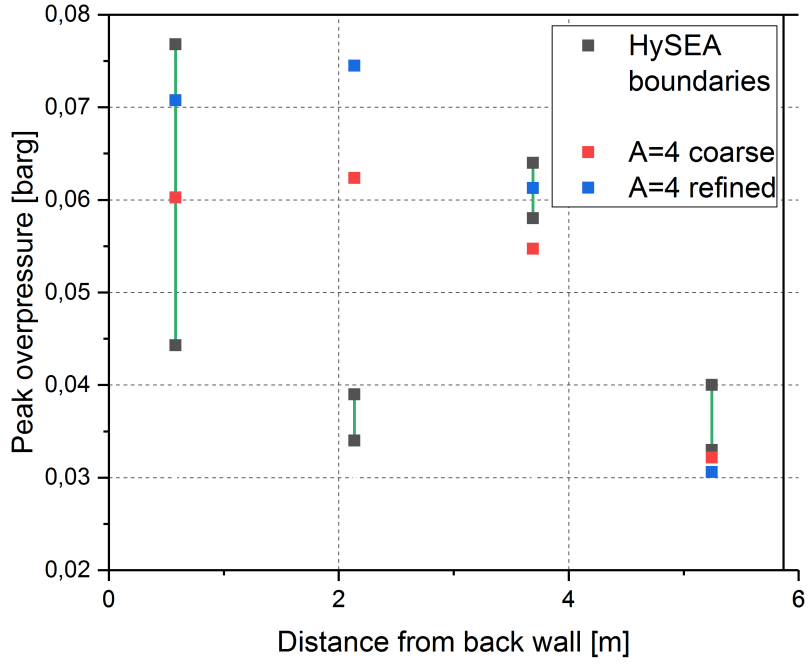

Figure 6.11: 'Artificial instability' with bottles: pressure vs. back wall distance

6.1.4 Lessons learned

The simulations carried out with the original COM3D version resulted in certain key insights, which can be assigned to low turbulence scenarios in general and the applicability of the code.
In particular the only partly successful turbulent calculations showed that directly after ignition, turbulence is still so underdeveloped that flame wrinkling must be caused mainly by instabilities. In this work, this effect is attributed to thermodiffusive effects, but could also be induced by other types of instabilities. In this early phase of combustion, the fluctuations are still below laminar flame speed ($u' < S_L$). In this case, the flame speed model by *University of Leeds* does not seem to be valid. This represents an important finding, which was not known before, as COM3D is usually applied for fast combustion scenarios, where significantly larger turbulence levels occur.
In general, the simulations showed that the experiments can be reproduced with the original COM3D code, regarding both pressure vs. time and vs. distance. However, all successful calculations required the determination of initially unknown parameters, such as the fixed flame speed S_t in subsection 6.1.1, the turbulence enhancing factor A and the transition radius R. This does not allow blind-predictions. For this reason, the code development presented in section 4.3 was initiated.

6.2 Modified COM3D code

Following the code development, further simulations have been performed. Figure 6.12 gives an overview of the three calculations discussed in this work.

Simulation	Flame speed	TDI
Without bottles	$S_{L,\text{eff}} = \Xi_{TDI}(R) S_L,$ $S_t = f(u', \dots)$	+
With bottles 1		+
With bottles 2		+

Figure 6.12: Simulations with the modified COM3D code

6.2.1 Simulation without bottles

According to the procedure introduced in section 4.3, the preliminary calculation with the modified model yielded a transition radius $R_{transition} = 2.0\ m$ for this set-up. Due to the lack of obstacles, such a relatively late development of turbulence seems still reasonable. The result of the actual simulation is displayed in Fig. 6.13. A comparison with the experiment shows good agreement regarding the pressure peak value. The location in time is shifted slightly, but still matches quite well. This time, the oscillations behind the major pressure peak are lower than in the simulations with the original code, but still within the measured range. The reduced intensity can be attributed to the model changes, where after a certain time, the effect of TDI is not considered anymore.

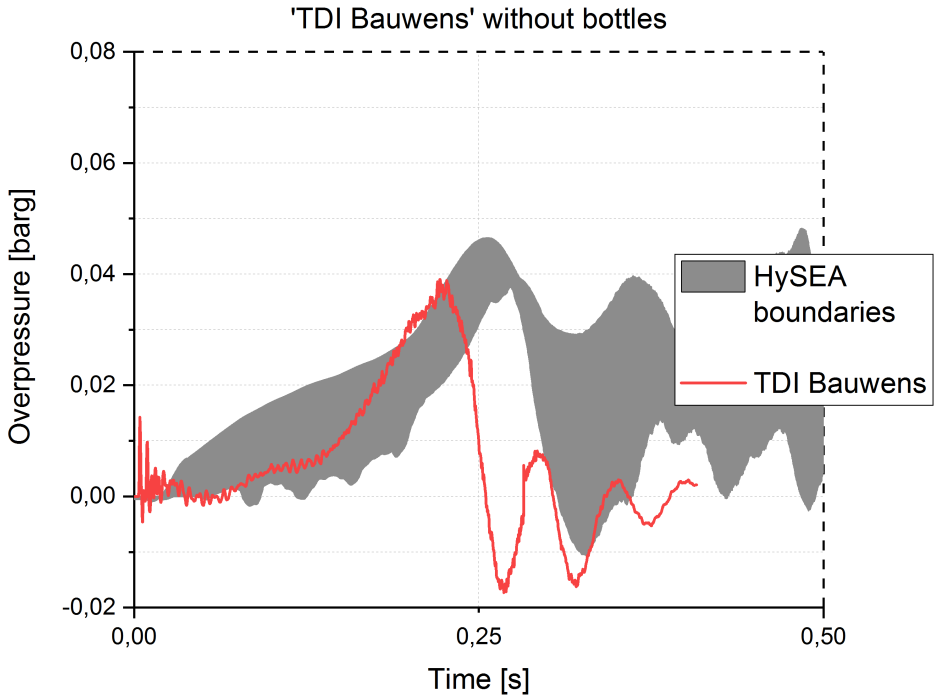

Figure 6.13: Modified code without bottles: pressure vs. time

Figure 6.14 depicts that the peak overpressure and the tendency of pressure vs. back wall distance is reproduced adequately. In addition to that, the decrease in pressure is more pronounced than for the previous calculation approaches, which results in a better match of experiment and simulation.
To conclude, the code modification proved to be successful for this configuration.

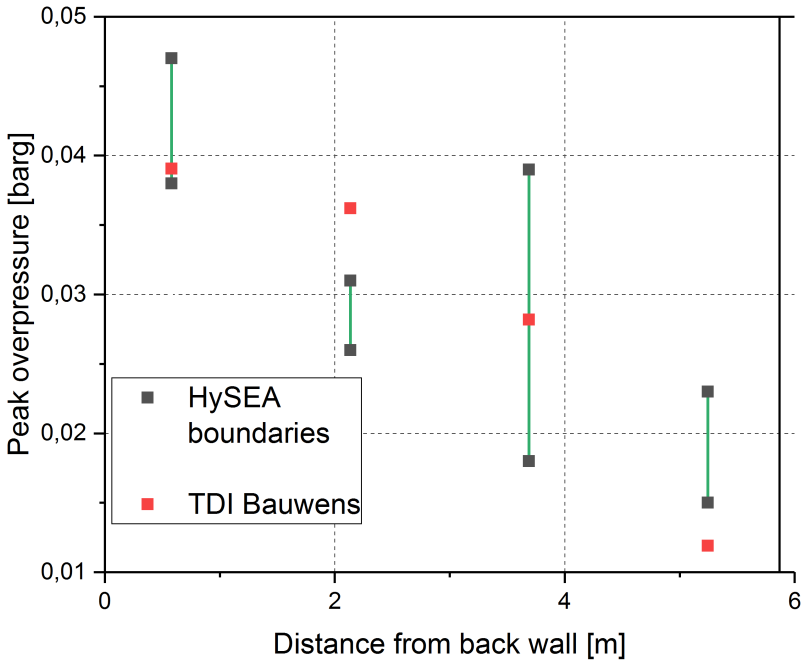

Figure 6.14: Modified code without bottles: pressure vs. back wall distance

6.2.2 Simulation with bottles

In case of the simulation with bottles, the flame front becomes heavily deformed due to the interaction with the obstacle. This makes the correct assessment of the laminar-turbulent transition more difficult. In particular with the currently used manual procedure, the radius at which the condition $u' = S_L$ is reached remains unclear to a certain point. Therefore, two different transition radii were tried out.
Figure 6.15 illustrates the results with $R = 1.0\ m$ (red curve) and $R = 1.3\ m$ (blue curve). Both approaches produce overly low overpressure values, with the condition $R = 1\ m$ also resulting in a different characteristic, that is the maximum value is reached at the second pressure peak. By enlarging the radius to $R = 1.3\ m$, the result is improved, but still unsatisfactory. Further increase of the radius could lead to better results. Owing to the time limitation of this work, subsequent simulations were not performed. With respect to future work, it is necessary to check if the transition condition $u' = S_L$ is still valid or whether it has to be replaced by another criterion. As the pressure history over time could not be reproduced satisfyingly, the curve pressure vs. distance is omitted.

In total, the code modifications have to be reviewed in order to also allow blind-predictions with obstacles.

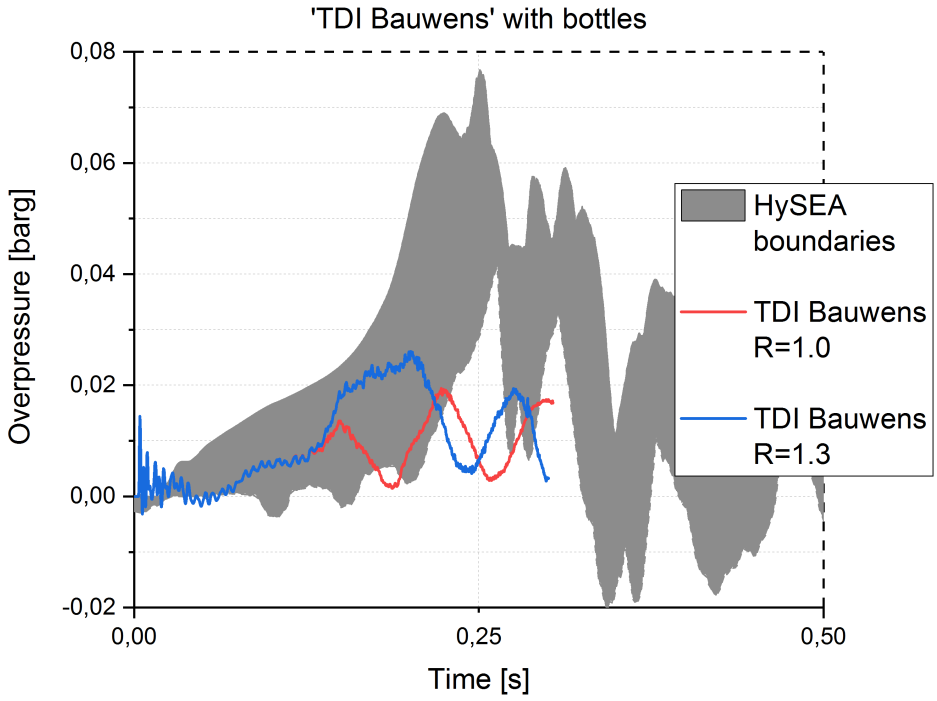

Figure 6.15: Modified code with bottles: pressure vs. time

6.3 Discussion

In subsection 6.1.4 and the previous section 6.2, the key insights of calculating with the original and the modified COM3D code are pointed out. This section merely summarizes the progress made while performing the simulations.

Figures 6.16 and 6.17 compare the HySEA results with the blind prediction, the 'Artificial instability' approach and 'TDI Bauwens', which denotes the suggested code modification, for both experimental set-ups. The peak overpressure was successfully reproduced by artificially increasing turbulent fluctuation (blue curves). Calculations with the modified code (green) yielded satisfying results for the scenario without obstacles, regarding both pressure vs. time and pressure vs. back wall distance (see Fig. 6.14).

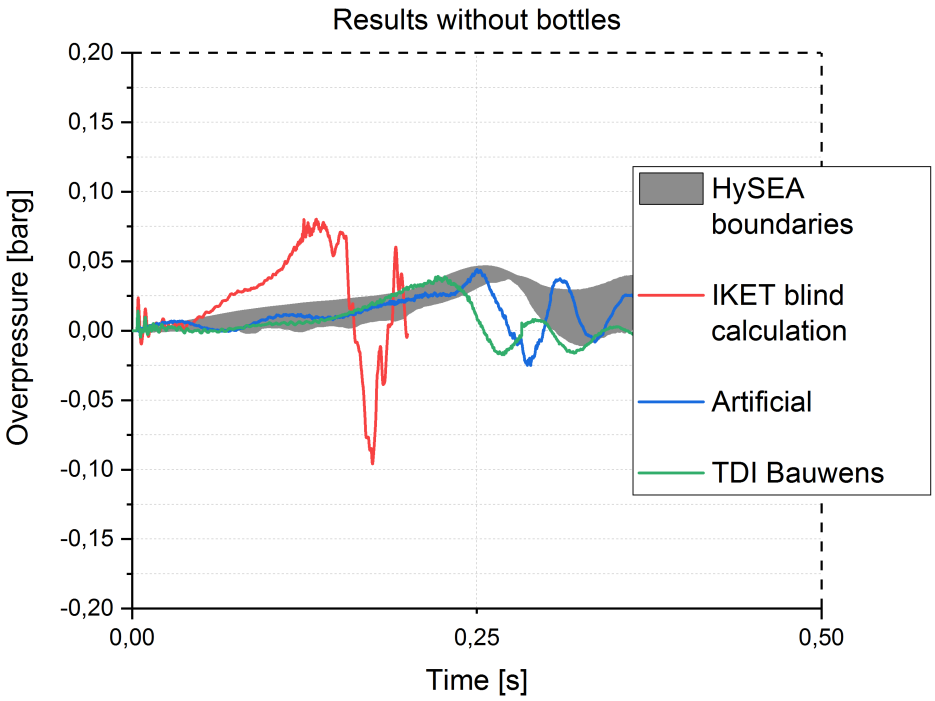

Figure 6.16: Results without bottles

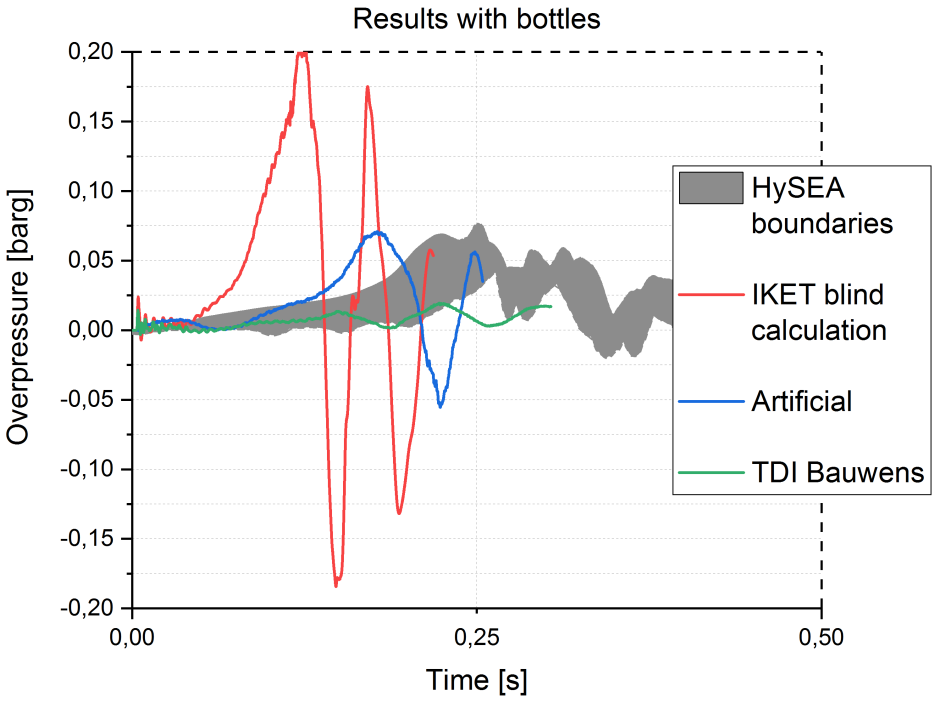

Figure 6.17: Results with bottles

7 Conclusion

7.1 Summary

This thesis deals with the numerical simulation of vented hydrogen combustion scenarios. The work included the following tasks:

- Introductory training in the CFD tool COM3D
- Analysis of the experimental data gathered by the HySEA project
- Simulation of two test cases with the orginal COM3D version
- Analysis and clarification of the mechanisms relevant to the considered combustion scenarios
- Code development including further simulations with the modified code
- Comparison of the simulation results with experimental data

By defining several calculation approaches, the main effects of the flame speed model and the role of thermodiffusive instabilities were investigated. In this context, the resulting maximum pressure loads of both experimental set-ups of the HySEA project could be reproduced with the original COM3D code. In order to enable blind-predictions in the future, code development was initiated. The changes suggested during this work proved to be successful for one of the combustion scenarios. This can be regarded as a first step towards extending the applicability and predictability of the COM3D code.

7.2 Future work

There are multiple starting points for further research in the topics treated in this work. They can be subdivided into two main categories, the code development in general and further activities related to the HySEA project.

The suggested code modifications showed progress for one specific combustion scenario. In order to obtain a more broadly applicable CFD code, the model for thermodiffusive instability has to be reviewed. Concretely, it might be tuned further or be replaced by another approach. In this context, changing the definition of the effective Lewis number also represents a possibility. Moreover, further effects could be included, such as a thermodiffusive mechanism which stabilizes the flame, thus leading to lower flame speeds. Regarding performance, the simulation procedure has to be simplified. This means that the preliminary calculation of the transition criterion should be included in the actual simulation.

With respect to the considered scenarios, the variation of the turbulence model to an LES approach could further improve the insight into the turbulent processes. Moreover, the HySEA project offers a large variety of additional experimental data for further code development and validation. The second experimental campaign of the project rounds off the study with a focus on inhomogeneous mixtures and initial turbulence. On this basis, the effect of different hydrogen concentrations, obstacles and vent configurations can be investigated.

References

[1] C. Bauwens, J. Bergthorson, and S. Dorofeev. Experimental investigation of spherical-flame acceleration in lean hydrogen-air mixtures. *International Journal of Hydrogen Energy*, 42(11):7691–7697, 2017.

[2] C. Bauwens, J. Chaffee, and S. Dorofeev. Experimental and numerical study of hydrogen–air deflagrations in a vented enclosure. 2008.

[3] C. R. Bauwens, J. Chaffee, and S. Dorofeev. Experimental and numerical study of methane-air deflagrations in a vented enclosure. *Fire Safety Science*, 9:1043–1054, 2008.

[4] C. R. Bauwens, J. Chao, and S. Dorofeev. Effect of hydrogen concentration on vented explosion overpressures from lean hydrogen-air deflagrations. *international journal of hydrogen energy*, 37(22):17599–17605, 2012.

[5] R. Borghi. Turbulent combustion modelling. *Progress in Energy and Combustion Science*, 14(4):245–292, 1988.

[6] D. Bradley, A. Lau, and M. Lawes. Flame stretch rate as a determinant of turbulent burning velocity. *Philosophical Transactions of the Royal Society of London A: Mathematical, Physical and Engineering Sciences*, 338(1650):359–387, 1992.

[7] T. Brutscher, N. Zarzalis, and H. Bockhorn. An experimentally based approach for the space-averaged laminar burning velocity used for modeling premixed turbulent combustion. *Proceedings of the Combustion Institute*, 29(2):1825–1832, 2002.

[8] G. Ciccarelli and S. Dorofeev. Flame acceleration and transition to detonation in ducts. *Progress in Energy and Combustion Science*, 34(4):499 – 550, 2008.

[9] J. F. Driscoll. Turbulent premixed combustion: Flamelet structure and its effect on turbulent burning velocities. *Progress in Energy and Combustion Science*, 34(1):91–134, 2008.

[10] A. Efimenko and S. Dorofeev. Crebcom code system for description of gaseous combustion. *Journal of Loss Prevention in the Process Industries*, 14(6):575 – 581, 2001.

[11] EN14994. Gas explosion venting protective systems, 2007.

[12] Y. A. Gostintsev, V. Fortov, and Y. V. Shatskikh. Self-similar propagation law and fractal structure of the surface of a free expanding turbulent spherical flame. In *Doklady Physical Chemistry*, volume 397, pages 141–144. Springer, 2004.

[13] T. Green-Book. Method for the determination of possible damage to people and objects resulting from releases of hazardous materials. *CPR 16E, CIP data of the Royal Library,*, 1992.

[14] Ö. L. Gülder. Turbulent premixed combustion modelling using fractal geometry. In *Symposium (International) on Combustion*, volume 23, pages 835–842. Elsevier, 1991.

[15] A. N. Kolmogorov. The local structure of turbulence in incompressible viscous fluid for very large reynolds numbers. In *Dokl. Akad. Nauk SSSR*, volume 30, pages 299–303, 1941.

[16] A. Kotchourko, A. Lelyakin, J. Yanez, G. Halmer, and A. Svishchev. *COM3D: Turbulent Combustion Code - User's Guide*, version 4.8 edition, 2014.

[17] M. Lecanu, K. Mehravaran, J. Fröhlich, H. Bockhorn, and D. Thévenin. Computations of premixed turbulent flames. *High Performance Computing in Science and Engineering07*, pages 229–239, 2008.

[18] B. Lewis and G. v. Elbe. *Combustion, flames and explosions of gases*. Acad. Pr., Orlando, Fla. [u.a.], 3. ed. edition, 1987.

[19] A. Lipatnikov and J. Chomiak. Turbulent flame speed and thickness: phenomenology, evaluation, and application in multi-dimensional simulations. *Progress in energy and combustion science*, 28(1):1–74, 2002.

[20] I. Matsukov, M. Kuznetsov, V. Alekseev, and S. Dorofeev. Photographic study of the characteristic regimes of turbulent flame propagation, local and global quenching in obstructed areas. Technical report, Report, 1998.

[21] V. Molkov. Accidental gaseous deflagrations: Modelling, scaling and mitigation. 12(7):19–30, 2002.

[22] NFPA68. Standard on explosion protection by deflagration venting, 2013.

[23] N. Peters. *Turbulent combustion*. Cambridge monographs on mechanics. Cambridge University Press, Cambridge [u.a.], repr. edition, 2004.

[24] B. Ponizy, A. Claverie, and B. Veyssière. Tulip flame-the mechanism of flame front inversion. *Combustion and Flame*, 161(12):3051–3062, 2014.

[25] B. Savard and G. Blanquart. An a priori model for the effective species lewis numbers in premixed turbulent flames. *Combustion and Flame*, 161(6):1547–1557, 2014.

[26] H.-P. Schmid, P. Habisreuther, and W. Leuckel. A model for calculating heat release in premixed turbulent flames. *Combustion and Flame*, 113(1):79–91, 1998.

[27] T. Skjold. Blind-prediction: estimating the consequences of vented hydrogen deflagrations for homogeneous mixtures in 20-foot iso containers. 2017.

[28] O. Sommersel, D. Bjerketvedt, S. Christensen, O. Krest, and K. Vaagsaether. Application of background oriented schlieren for quantitative measurements of shock waves from explosions. *Shock Waves*, 18(4):291–297, 2008.

[29] O. Sommersel, K. Vaagsaether, and D. Bjerketvedt. Hydrogen explosions in 20-foot iso container. *International Journal of Hydrogen Energy*, 42(11):7740–7748, 2017.

[30] J. Warnatz, U. Maas, and R. W. Dibble. *Combustion : physical and chemical fundamentals, modeling and simulation, experiments, pollutant formation; with ... 22 tab.* Springer, Berlin, 4. ed. edition, 2006. Gb. : EUR 58.80 (freier Pr.), ca. sfr 88.50 (freier Pr.).

[31] J. Yáñez. *A model for turbulent simulation of large scale hydrogen explosions*. PhD thesis, 2015.

[32] Y. B. Zel'dovich, V. Librovich, G. Mahviladze, and G. Sivashinsky. On the detonation formation in a non-uniformly preheated gas. *Journal of Applied Mathematics and Technical Physics*, 2:76–84, 1970.

[33] V. Zimont. To computations of turbulent combustion of partially premixed gases. *Chemical Physics of Combustion and Explosion Processes. Combustion of Multi-Phase and Gas Systems*, pages 77–80, 1977.